**GEOLOGY FOR SOCIETY**

SINCE 1858

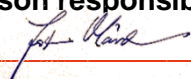GEOLOGICAL
SURVEY OF
NORWAY

· NGU ·

# REPORT
## GEOLOGY FOR SOCIETY

GEOLOGICAL SURVEY OF NORWAY
- NGU -

| Report no.: 2020.013 | **ISSN:** 0800-3416 (trykt) | |
|---|---|---|
| | **ISSN:** 2387-3515 (online) | **Grading:** Open |
| **Title:** Moho topography and velocity/density model for the Hedmarken area, eastern Norway | | |
| **Authors:** Pavez, Claudia; Brönner, Marco; Bjørlykke, Arne; Olesen, Odleiv. | **Client:** NGU | |
| **County:** Oslo, Innlandet | **Municipality:** Gjøvik | |
| **Map-sheet name (M=1:250.000)** | **Map-sheet no. and -name (M=1:50.000)** | |
| **Deposit name and grid-reference:** | **Number of pages:** 43 **Price (NOK):** 120 | |

| Fieldwork carried out: | Date of report: 1 April 2020 | Project no.: 362200 | Person responsible: |
|---|---|---|---|

**Summary:** A Receiver Function Analysis was carried out in the Hedmark area, Eastern Norway, in order to understand the current crustal composition and complement geological analysis that were made previously in the area. For this, we have used tele-seismic recordings from seven broadband stations that belong to the NORSAR permanent array. One main intra-crustal discontinuity related to high reverberations between the direct P phase and the Moho Ps conversion can be derived from the stacked receiver functions under the western stations. We interpret this discontinuity in connection with the Åsta basin. The Hκ (depth vs Vp/Vs) stacking procedure allows us to obtain a model with the Mohorovicic discontinuity values under each seismic station, the average Vp/Vs crustal ratio and the Poisson's ratio. The Moho depth presents variations increasing its values to the northeast of the study area, where the thickest crust was found (~38.5 km) and in agreement with the Moho depths of previous research in southern Norway. With respect to the parameters, the Vp/Vs and the Poisson's ratios have the expected values according to the local geology, as they explain well an average felsic crustal composition and the presence of metasediments in the Åsta basin (Vp/Vs = 1.71-1.73 & $\sigma \sim 0.24$) and the granitic composition with mafic intrusions to the east of the study area (Vp/Vs = 1.78-1.79 & $\sigma \sim 0.27$). These results are supported by high magnetic anomalies associated to mafic Pre-Sveconorwegian and Sveconorwegian intrusive bodies and to low anomalies correlated to the thickness of the Åsta basin deposits. As an independent method and using a transdimensional inversion algorithm we obtained a 1D local velocity model. Applying the Nafe-Drake relationship, a 2D density model was obtained and tested against observed gravity. Results indicate the presence of a low anomalous density layer that is located to the NNW of the study area, which is probably related to low-density meta-sediments of the Åsta basin which are located above the Mesoproterozoic basement. A main crustal fault is also indicated from the density model, spatially coinciding with faults grown during the Sveconorwegian orogenic process.

| Keywords: Receiver function analysis | Transdimensional inversion | NORSAR teleseismic recordings |
|---|---|---|
| Hκ stacking method | Density & gravity models | Markov chain Monte Carlo inversion |

Table of Contents

**Figures and Tables**

# 1. INTRODUCTION

Knowledge of the structure of the continental crust and upper mantle is fundamental to understand genesis, evolution, and current geological processes occurring at local or regional scales in a defined area. A variety of geophysical methods provide an important framework for our understanding, such as the forward/inverse imaging techniques, with a great development during the last two decades (Zhao, 2007 *and references there in*). In this context, several geophysical studies such as seismic tomography (Köhler et al, 2011, 2012), active source seismic refraction (Kanestrøm & Haugland, 1971; Sellevoll & Warrick, 1971; Kanestrøm & Nedland, 1975; Mykkelveit, 1980; Stratford & Thybo, 2011a, 2011b) and receiver function analysis (Svenningsen et al., 2007; Frasetto & Thybo, 2013; Kolstrup & Maupin, 2013; Ottemöller & Midzi, 2003) have provided comprehensive insights in the lithospheric structure for southern Norway. Likewise, magnetotelluric, magnetic and gravity models can be found elsewhere in the literature, some of them compiled by Olesen et al. (2010a, b, c) and Ebbing et al. (2012). In general, all these results reveal clear Moho discontinuities and a fairly homogeneous crust with only small intra-crustal velocity variations.

Specifically, receiver functions are the deconvolved P to S conversions of tele-seismic waves at sub-horizontal crustal-upper mantle discontinuities (Ammon et al., 1990; Ammon, 1991). Because of this natural conversion, they constitute a very useful technique to find detectable interfaces such as intra-crustal discontinuities or major velocity transition zones. This estimation, which is based on the time separation between the direct P arrival and the conversion phase Ps, provides good measurements of the crustal thickness under the station because of the steep incident angle of the teleseismic P wave (Zhu & Kanamori, 2000). With this respect, the HK (depth - Vp/Vs) stacking method, which considers the summation of several individual receiver functions, is the most used approach as it allows to find simultaneously the Moho depth as well as the Vp/Vs values and the Poisson's ratio (Zhu & Kanamori, 2000). Both ratios can add constraints about the crustal average rock composition and how it varies regionally (Zandt & Ammon, 1995; Stratford & Thybo, 2008b). Regarding the Moho depth in the European plate and particularly in Norway, the main compilations can be found in Kinck et al. (1993), Tessauro et al. (2007), Grad et al. (2009) and Stratford et al. (2009).

When the dimension of the model space is an unknown, we refer to a transdimensional inversion problem (Bodin et al., 2012), firstly used in earth sciences by Malinverno, (2002). Eight years later, the first application of a transdimensional algorithm was used for receiver function analysis (Piana-Agostinetti & Malinverno, 2010), developed to obtain Vs velocity models and elastic parameters. One of the most recent tools to invert seismic receiver functions corresponds to the *Reverse jumping Markov chain Monte Carlo* (Rj-McMC) method (Gallagher et al., 2009; Green, 1995, 2003; Malinverno, 2002;

Piana-Agostinetti & Malinverno, 2010; Bodin et al., 2012;  Sambridge et al., 2013). This approach allows to generate a sequence of models through a chain structure. Each model is a perturbation of the last one, producing a proposed model, which is accepted or rejected according to the acceptance criterion (Bodin et al., 2012). In this way, at the end of the iterative process, the final result corresponds to an ensemble of solutions. In the case of transdimensional receiver function inversion the unknowns are the velocity model as well as the number of different layers and how these ones are distributed along the crust.

Most of the abovementioned studies are focused into developing regional analysis, covering extensive areas. This is the case of receiver function studies for southern Norway than can be found for example in Frasetto & Thybo (2013), and in Kolstrup & Maupin (2013). However, the analysis of smaller areas can be also useful to understand and interpret local features, which details could complement regional results.  In this report we present a receiver function analysis for the Hedmark area, Innlandet, Eastern Norway, in order to understand the crustal structure underneath seven seismic stations corresponding to the large aperture NORSAR seismic array (Figure 1). The Moho topography values and the Vp/Vs ratios obtained by using the HK stacking method under each station, are used to better understand the correlation between the observable local geology and the non-observable crustal features, and how are these related with the current configuration of the rock composition in the area. Independently, a 1D S-wave velocity model obtained from a Rj-McMC inversion was then calculated to generate a 2D local density model, using the Nafe-Drake $\rho$(Vp) relationship. Our main goal consists in corroborating previously available information about the area and understand the local geology, which is tectonically related with the Caledonian orogenic front.

**Table 1: NORSAR array geographic coordinates, elevation and station codes**

| Station code | Latitude [°] | Longitude [°] | Elevation [m] |
|---|---|---|---|
| NAO01 | 60.844 | 10.886 | 426 |
| NBO00 | 61.030 | 10.777 | 529 |
| NC204 | 61.275 | 10.762 | 851 |
| NC602 | 60.735 | 11.541 | 305 |
| NB201 | 61.049 | 11.293 | 613 |
| NC405 | 61.112 | 11.715 | 496 |
| NC303 | 61.225 | 11.369 | 401 |
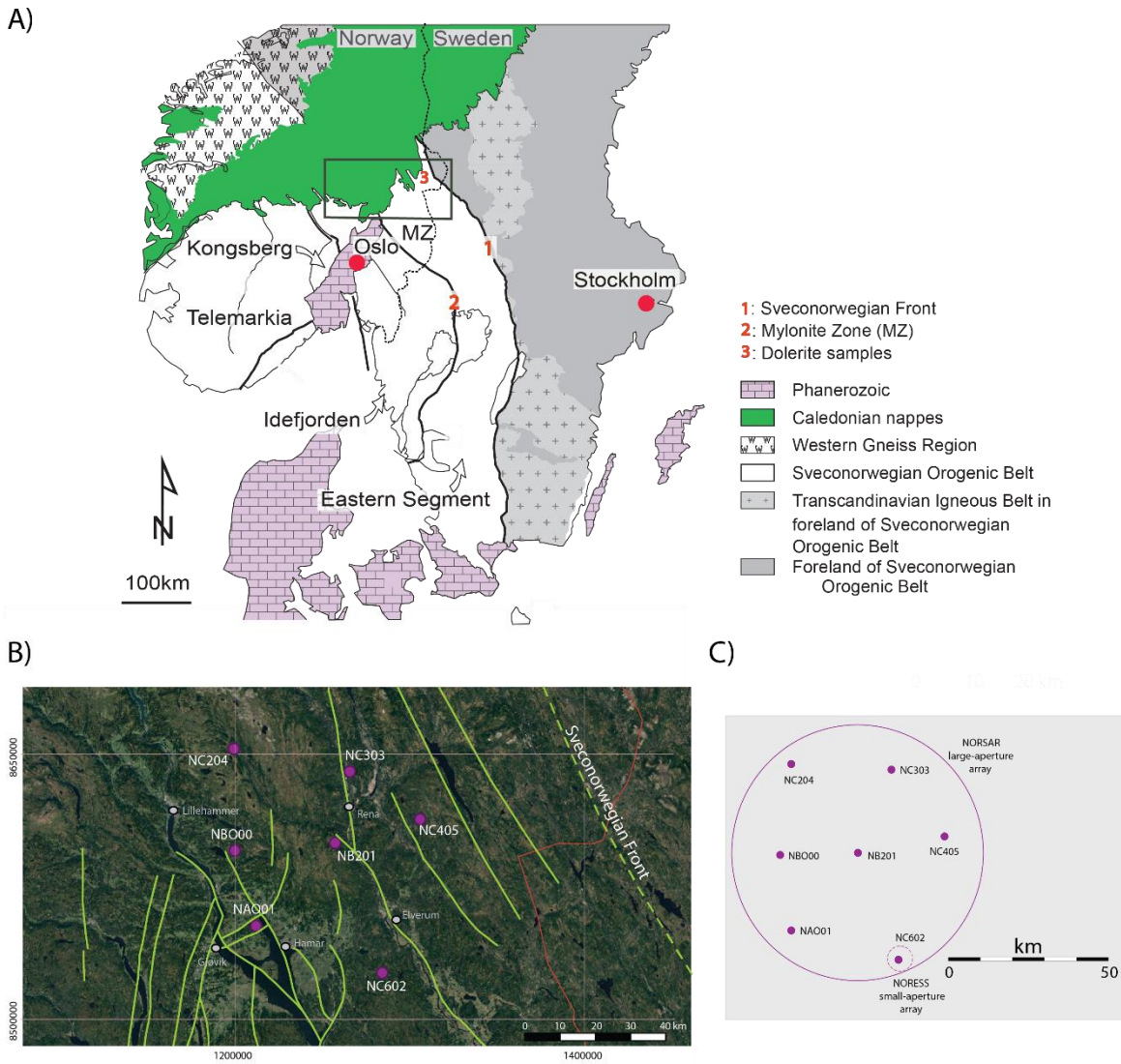
*Figure 1. A). Sketch map showing the lithotectonic units of the Sveconorwegian Orogenic Belt (Modified from Bingen & Viola, 2018). The black box is showing the location of the NORSAR array and the interpolation area used in this research B). Digital elevation model showing a zoom-in of the seismic stations. Green lines correspond to the major faults observed in the zone, mainly composed by NS and NNW lineaments near to the array. Dotted green line delineates the Sveconorwegian front. C). Geometry and size of the NORSAR array. The NORESS small-aperture array is shown, co-located with the NC602 station (modified from Schweitzer & Roth, 2015).*

## 2. GEOLOGICAL SETTING & SEISMIC CRUSTAL STRUCTURE

The bedrock geology of southeastern Norway is mainly composed by a Mesoproterozoic basement (Bingen et al., 2008a) partly covered by an autochthonous Cambro-Silurian metasedimentary layer (Bjørlykke & Olesen, 2018). The Precambrian basement is constituted of the Transscandinavian Igneous Belt to the east (TIB; 1.86 – 1.66 Ga), followed by the old eastern segment of the Idefjorden Lithotectonic unit (IDL; 1.64 – 1.52 Ga) and the Telemarkia Lithotectonic unit (TLU; 1.52 – 1.48 Ga) to the west (Figure 1A). At the end of the Mesoproterozoic (1.14 – 0.97 Ga) the Sveconorwegian

orogeny produced a *c.* 500 km wide orogenic belt extending across the Baltic shield, with an extensive Sveconorwegian Frontal Deformation Zone (SFDZ) to the east (Figure 1A) (Bingen et al., 2008a; Möller et al., 2015). Between the TIB and the IDL there is a major Sveconorwegian mylonite zone which corresponds to the Mjøsa area. This mylonite zone of around 450 km length, separates the eastern segment from allochthonous units to the west (Figure 1A). To the east of Mjøsa, the SFDZ is located (Bjørlykke & Olesen, 2018) (Figure 1A).

Meso- to Neoproterozoic (1.6 – 0.9 Ga) dolerite dykes and sills were reported on and to the east of the SFDZ by Söderland et al., (2005, 2006). Some of the samples belongs to the pre-Sveconorwegian interval (1.34-1.14 Ga), as is the case of the extensive Central Scandinavian Dolerite Group (CSDG) (Bingen et al., 2008a; Söderlund et al., 2005; Söderlund et al., 2006). Meanwhile, the Blekinge-Dalarna dolerites include samples recorded at the Caledonian front of ages at $978 \pm 1.8$ Ma, and which rocks represent exceptions to the large-scale felsic magmatism related to the Sveconorwegian orogeny (Möller et al., 2005) (Figure 1A).

The basement-metasedimentary sequence is cut by the Caledonian nappes. The Scandinavian Caledonides are subdivided into four levels, which were transported to the east onto the Fennoscandian platform (Bingen et al., 2008a). These levels are the Lower, Middle, Upper and Uppermost allochthons, which are in turn composed by several nappe complexes (Gee et al., 2010; Lamminen et al., 2015; Roberts & Gee, 1985; Roberts, 2003). The Lower and Middle allochthons are generally considered endemic to Fennoscandia before the Caledonian orogeny. On the contrary, the Upper and Uppermost allochthons are considered related to the Iapetus Ocean or Laurentian terrains (Bingen et al., 2008a).

To the northwest of the study area the Åsta basin is located (Figure 1A & 1B), which is constituted of up to c. 1.5 km thick meta-sandstones in addition to dolomites and shales in the Middle and Lower Allochthon. The thickness of the nappes and consequently of the basin was previously estimated to a maximum of c. 4 km (Nystuen, 1981; Skilbrei et al., 2002; Olesen et al., 2007; Bjørlykke & Olesen, 2018).

Major tectonic faults, NS and NNW lineaments are clearly identified in the basement. These faults dominated the tectonic evolution in the Neoproterozoic to Early Cambrian and during the Permian (Bjørlykke & Olesen, 2018; Gabrielsen et al., 2018; Laminnen et al., 2015) (Figure 1B).

Regarding the crustal seismic structure beneath the Southern Scandes, a very comprehensive analysis was published by Stratford & Thybo (2011a). P- and S-wave velocities, Poisson's ratio, density and composition (%SiO2) are presented in 1D models under Southern Norway. Particularly, Poisson's values range between 0.24 to 0.27 and the $SiO_2$ percentage from 64% to 72%. The average crustal density was estimated in 2,800 kg/m$^3$. With respect to S-wave velocities, the values vary between 3.2 to 4.6 km/s from the surface to 40 km depth (Stratford & Thybo, 2011b).

Previous seismic research in the study area was published by Ruud & Husebye (1991), using the NORESS array records. NORESS was a small aperture array - 3 km - which was located circularly around the NC602 seismic station (Figure 1C). The P-wavefield complexities were imaged and results indicated a relatively homogeneous area to the southwest with granite/rhyolite composition bedrocks, meanwhile, to the northeast the presence of an intrusive gabbro body was detected.

Several authors have described and calculated the crustal thickness for southern Norway (Kinck et al., 1993; Svenningsen et al., 2007; Tesauro et al., 2007; Grad et al., 2009; Stratford et al., 2009; Stratford & Thybo, 2011; Ebbing et al., 2012; Frasetto & Thybo, 2013; Kolstrup & Maupin, 2013). Grad et al. (2009), developed a European Plate Moho depth map using a compilation of data that contains available recent and high-quality seismic results on the crustal structure. This map indicates for the study area a Moho depth between 30 – 40 km, increasing to the NE. After Grad et al. (2009) and Stratford et al. (2009), updated models in the Southern Scandes area (Ebbing et al., 2012), are showing the behavior of the crustal thickness from the coast to inland. To the north of the Oslo Rift where the crust reaches c. 30 km depth, it continues to thicken eastwards, to more than 50 km beneath the central Fennoscandian Shield (see Fig. 8 in Ebbing et al., 2012).

## 3. METHODOLOGY

### 3.1. Data source and processing

Seismic stations are part of the NORSAR permanent network composed by seven broadband, three-component and continuous recording equipment, model CMG-3T-Hybrid. Seismic data were obtained from the IRIS catalogue, which is available online, using Wilber3 for event selection and extraction. A total number of 50 seismic events recorded during the 2017-2018 period were analyzed. After removing the bad quality traces, a set of 20 high magnitude events ($Mw \geq 6.0$, $Mb \geq 5.6$) with epicentral distances between 30° - 90° were selected (Figure 2). In additional to the signal quality, the events were selected seeking for those heterogeneously distributed around the network. For those cases where the Mb magnitude was the only one available, the magnitude conversion between Mw – Mb was made using the empirical global relation described by Lolli et al, 2014 (Equation 1):

$$M_w = exp(0.741 + 0.210\, mb) - 0.785 \qquad (1)$$

The ray parameter (p) was calculated for each event, using the UDTDD software available in the CPS (Computer Software for Seismology) package (Hermann, 2013).

*Figure 2. Location of teleseismic events accepted for processing and stacking (red stars). All the events are located between 30° - 90° from the study area, centered at NB201 seismic station (blue triangle)*

## 3.2.  Receiver function calculation

Receiver functions allow to isolate the P to S conversions generated in crustal and crustal-mantle transitions by source equalization. The natural conversion occurs at the Moho, however, the variations in density and elastic parameters beneath the seismic stations also generate intra-crustal interfaces (Fontaine et al., 2015), for example, in sedimentary layers. In RFA, the input data are broadband three-component observations of teleseismic P-waves (Ammon et al., 1990; Ammon, 1991) from the earthquakes at epicentral distances between 30° and 90°.  The waveform is a composite of P- to S-converted waves that reverberate in the structure beneath the seismometer. Isolating the local response requires deconvolution (Clayton & Wiggins, 1976; Ammon, 1991) which can be done in frequency or time domain.

The time separation between P to Ps waves is then useful to estimate the crustal thickness H given the ray parameter (p) and the average P and S waves crustal velocities according to Equation 2 (Zhu & Kanamori, 2000).

$$H = \frac{t_{P_S}}{\sqrt{\frac{1}{V_s^2} - p^2} - \sqrt{\frac{1}{V_P^2} - p^2}} \qquad (2)$$

In general, using just a single receiver function it is very difficult to obtain an accurate crustal thickness, mainly due to the background noise and scatterings from crustal heterogeneities. In order to increase the signal to noise ratio, the best option is to use several seismic traces to finally stack their receiver functions in the time domain. Once the stacking is done, the solution trace will be in the HK domain, and expressed by the function $s(H, K)$ in Equation 3 (Zhu & Kanamori, 2000):

$$s(H, K) = \omega_1 r(t_1) + \omega_2 r(t_2) - \omega_3 r(t_3) \qquad (3)$$

Here r(t) is the radial receiver function; $t_1$, $t_2$ and $t_3$ are the predicted Ps, PpPs, and PpSs+PsPs arrival times corresponding to the crustal thickness and K=Vp/Vs. The $s(H, K)$ function reaches a maximum when all three phases are stacked coherently with the correct H and K. Finally, $\omega_i$ values are corresponding to the weighting factors for each multiple (Zhu & Kanamori, 2000).

For the selected events, all three components were synchronized and cut for the same time window. Mean and trend were removed, and a taper filter was also applied to remove the amplitudes at the end and the beginning of the signal. The second step was to rotate the signals to radial and tangential forms. Then, the RFs were calculated using the Iterative Time Domain Deconvolution (Ligorria & Ammon, 1999) available in the CPS package (Hermann, 2013) for the radial component. After testing, the selected Gaussian parameter was *a=3.0,* corresponding to a gain of 0.1 at approximately 1.5 Hz. This step removed the high frequency noise to better define the spikes of interest, including those corresponding to the intracrustal discontinuities. Previous works also show the usefulness of this value (*e.g* Ottemöller & Midzi, 2003) and additionally, Gaussian values above 2.0 seems to better capture the wiggles related with intracrustal variations (Zheng et al., 2005; Srinivas et al., 2013). The calculation of the receiver functions comprised *1000* iterations and a tolerance error equal to *0.0001%,* which allowed us to reproduce higher percentages of the signal. In our case, this percentage acts as the first quality criterion to select the RF's that were finally used to the stacking: only deconvolutions resulting in a receiver function reproducing more than *70%* of the signal were accepted. When selecting this value, the problematic deconvolutions identified with the misfit between the observed radial trace and the receiver function deconvolved with the observed vertical seismogram were removed. As a second criterion, the coherent signals were selected through a visual inspection in the record stack. Finally, to determine an observed RF for each station, the selected signals were stacked using the Signal Stacking Subprocess (SSS) routine available in SAC. This routine, among other features, allows to plot the

processed signal with or without the summation process, making a signal inspection possible in order to easily remove the undesirable traces.

To ensure that the structure beneath each station is 1-dimensional, two tests were performed. For all seismic station arrival times were plotted *vs* back azimuth for station NB201 and also *vs* **p** ray parameter (Figures S1 & S2 in Supplementary Material). According to this, there are no noticeable variations in the receiver function phases.

### 3.3. Hκ stacking calculation

Individual receiver functions were used in the SAC Hκ subroutine (Helffrich et al., 2013). This routine considers as inputs the individual ray parameters (*p)* and a Vp average crustal velocity. In the same way, weighting factors for each multiple were assigned, and minimum and maximum values for H and κ were selected. For the present study, *p* was calculated per event, Vp was set as 6.2 km/s, minimizing the RMS during the Hκ stacking process, and the weighting factors were 0.5, 0.4 and 0.1, respectively. These values represent the weights for the direct P-to-S conversion, Ps, and the reverberations PpPs and PsPs + PpSs. At last, the selected ranges were 20 < H < 50 and 1.5 < κ < 2.0 for the crustal thickness and Vp/Vs ratio, respectively.

### 3.4. Inversion procedure

Transdimensional inversion is the name given to the method that solves inverse problems treating model parameters as an unknown. By extending fixed dimensional inverse problems into transdimensional, it is possible to use the data themselves to constrain the results, more than specifying *a priori* conditions (Sambridge et al., 2013). In transdimensional inversion, the model is expanded in terms of a variable number of basic functions whose position and coefficients are unknowns. Equation 4 describes this in general: $m(x)$ represents the physical quantity of interest to be constrained by the data, which is a function of spatial position $x$. In the case of receiver functions, $m_i(x)$ corresponds to the wave speed, $\Phi_i(x)$ are the $i^{th}$ basis functions, and $k$ is the total number of unknowns or:

$$m(x) = \sum_{i=1}^{k} m_i \Phi_i(x) \qquad (4)$$

Following a Bayesian approach, the information and results are presented as probability distributions. The problem starts with a prior probability density function on the unknowns $p(m)$. Next, a likelihood function $p(d|m)$ is defined as the probability of the observed data given the model. In this way, a

sequence of models is generated in a chain, where the last model is a perturbation of the previous one. The Bayesian models link the above mentioned with a posterior density function, given by Equation 5:

$$p(m|d) = \lambda \, p(d|m) \, p(m) \qquad (5)$$

where $\lambda$ is a constant that measures the validity of the assumptions during the construction of the model. The solution to this formulation is not one optimum model, but an ensemble of them considering the entire posterior density function (Sambridge et al., 2013). All the sampled models have a defined parameterization given by the number and position of their interfaces. When a large number of models are averaged, these interfaces tend to overlap, better defining the ensemble model (Bodin et al., 2012). We will not go into the details of the formulation, that are beyond of this research and can be found in many previous studies (Bayes, 1763; Green, 1995, 2003; Malinverno, 2002; Gallagher et al., 2009; Agostinetti & Malinverno, 2010; Bodin et al., 2012; Fontaine et al., 2015).

In the present paper, the posterior probability function was calculated using the inversion code Rj-rf (Reversible jump– receiver function) with the Rj-McMC (Reversible jump – Markov chain Monte Carlo) library, both Fortran codes, which allows to run 1D or 2D spatial regression problems (iEarth codes, see references) (Denison et al., 2002; Gallagher et al., 2011; Sambridge et al., 2013). This is a software for inversion of seismic receiver functions to obtain the 1D shear wave velocity structure under each station using the reversible jump Markov chain Monte Carlo algorithm (Bodin et al., 2012). The number of iterations is initially fixed. At each step, a model is proposed, and it can be accepted or rejected in the ensemble solution. The first part of the chain (the burn-in period) is discarded, in order to do the model stationary and to reproduce an important sampling of the model space (Fontaine et al., 2015).

### 3.4.1. Model parameterization

Following the methodology proposed by Bodin et al., 2012, the radial receiver function is assumed to be dominated by the response of homogeneous horizontal layers beneath the seismic stations. The different phases are temporally determined by the first P arrival, so they are very sensitive to the variation of Vs relative to Vp (Bodin et al., 2012). For this reason, the Vp/Vs ratio is fixed to a reference model and equal to 1.76, allowing to invert only for Vs in each layer, which is in turn represented by a constant velocity in the final model.

The average receiver function considering all selected events was used as an entry data vector in the Rj-rf code. This code allows a maximum of 200 points to read and invert the receiver function file, so the original trace was re-sampled considering a number of interpolation points *NPTS = 200.* Initially, it is possible to fix the number of iterations, the burn-in period, and the maximum number of layers of

different velocities. Additionally, minimum and maximum Vs velocities must be added in order to obtain credible values according to local geology, setting a search range which define the model space (Table 2). With respect to this point, and as a constraint for the velocity model, density measurements from surface specimens were used (Ebbing et al., 2012), providing starting Vs values which are considered for the first layer between 0 and 0.2 km depth. Also, a maximum depth as well as the plausible Vs search range were taken from previous research developed in the area and studied for each station when possible (Table 2) (Kanestrøm, 1973; Kosarev et al., 1987; Ottemöller & Midzi, 2003; Svenningsen et al., 2007; Stratford & Thybo, 2011; Ebbing et al., 2012; Kolstrup & Maupin, 2013).

During the creation of a model, a new value of Vs is calculated by perturbing the previous one, adding it a random Gaussian value with a mean of 0 and standard deviation *vs_std* (Table 2). The same process is done to find a new Vs value during the creation of a new partition, in which case the value of *vs_std_layer* is used. By last, a noise scaling parameter range ($\sigma_{min}$ and $\sigma_{max}$) is utilized to consider observational uncertainties, as well as deconvolution and theory errors (Bodin et al., 2012) (Table 2). The interface depths between layers and the Vs wave velocity in each layer are unknowns, therefore they are found during the inversion. As a main result, the 1D S wave velocity profile as a function of depth is obtained.

**Table 2: Input parameters used in the RF-Rj inversion**

| Parameters | Value |
| --- | --- |
| Number of iterations | 80000 |
| Burn-in period | 10000 iterations |
| Depth | 0 – 40 km |
| Vs | 3.30 – 4.50 km/s |
| Maximum number of partitions (layers) | 35, 15, 5 for models 1, 2 and 3, respectively |
| Perturbation standard deviation for Vs (*vs_std*) | 0.01 - 0.04 |
| Perturbation standard deviation for Vs in a new layer (*vs_std_layer*) | 0.01 - 0.04 |
| $\sigma_{min}$ - $\sigma_{max}$ | 0.001-0.05 |

## 4.  RESULTS & DISCUSSION

### 4.1.  Hκ stacking results

The retrieved receiver functions are shown for all seismic stations in Figure 3. The selected weighting factors used during the stacking allow a clear identification of the reverberant phases, particularly regarding our interest to estimate the Mohorovicic interface ($\omega = 0.5$). The earliest Moho Ps arrivals (~3.5 – 4.0 s) are observed for NAO01 and NBO00, where the thinnest crust was found (Table 3) agreeing with the results obtained by Svenningsen et al. (2007). For all stations, except for NC602, the Moho Ps phases are clearly exposed around 4 to 5 seconds, indicating a well-defined Moho transition (Figure 3).
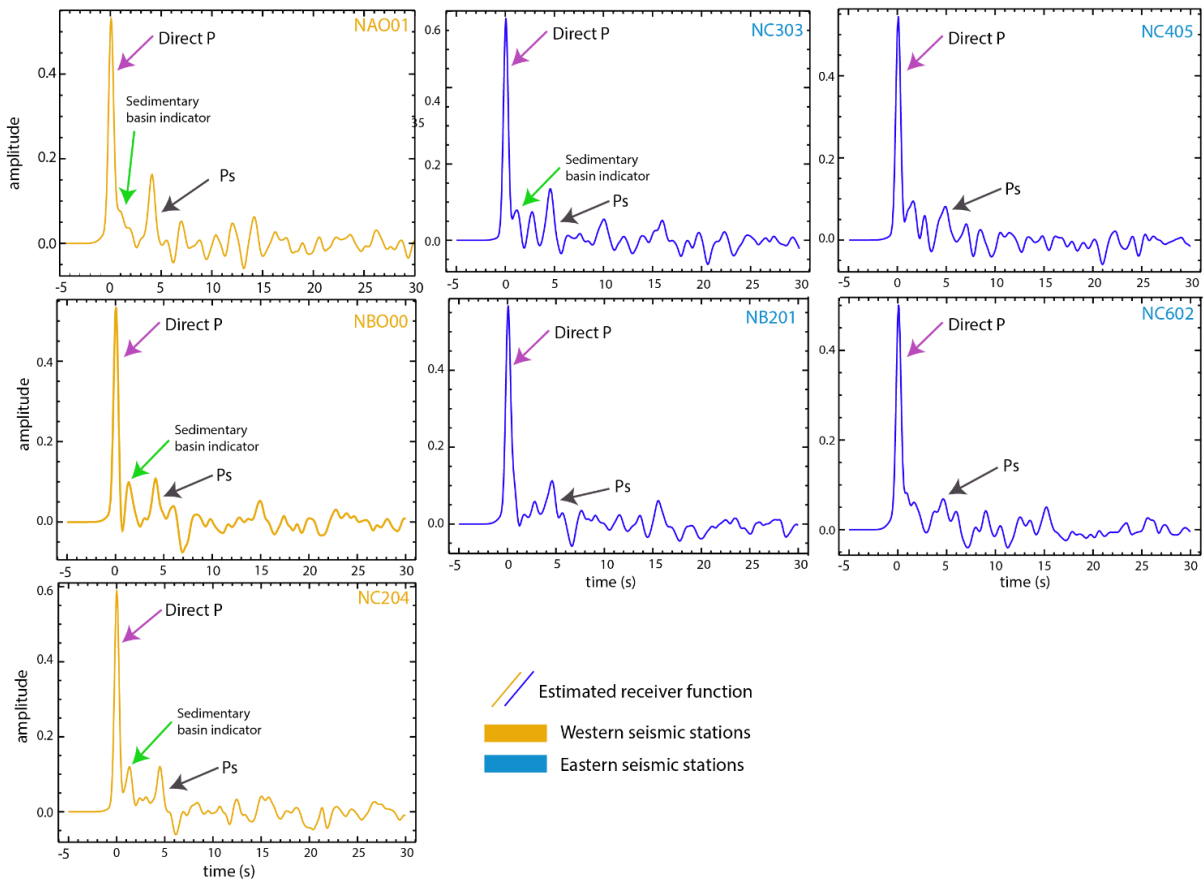


Figure 3: Stacked & non-scaled receiver functions for each seismic station. The main phases are shown and the intra-crustal discontinuities related to the Åsta basin are marked with a green arrow.

Stations located above the sedimentary layer have strong sedimentary reverberations (Figure 4), and in some cases a smaller positive wiggle can be observed before the Moho, clearly identifiable around 1 to 2 seconds in NBO00 and NC204 seismic stations (green arrows). Also, it is possible to identify a small positive variation in stations NAO01 and NC303. In general, these phases mark intra-crustal

16

discontinuities, which in this case can be associated with the Åsta basin. Similar results have been obtained in other sedimentary basins by inverting receiver functions (Rindraharisaona et al., 2017).
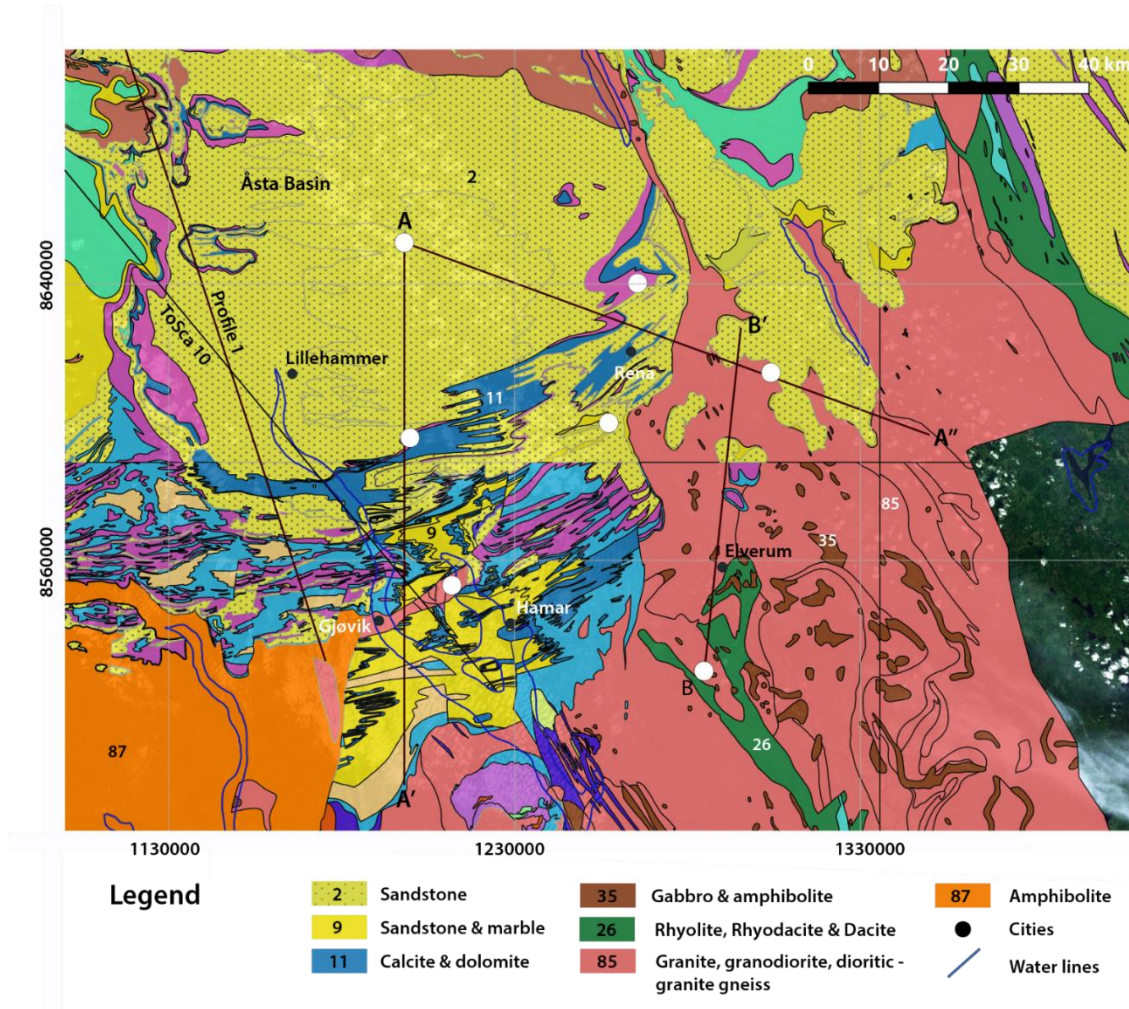


*Figure 4. Geological map of the Mjøsa area (1:1000000) over the digital elevation map. Grey dots are showing the NORSAR seismic array. Lithology codes are the same used in the Norwegian geological map, that can be found and downloaded in the NGU website (www.ngu.no).*

The obtained results for the Moho depth beneath each station are shown in Table 3 and Figure 5. To organize and compare the results, the stations were clustered in a western (orange) and eastern group (blue). For the western cluster, the crustal thickness increases to the north, whilst for the eastern the crust is thickening to the northeast (Table 3 & Figure 5). These results agree with those presented by Grad et al. (2009). As a general tendency, the Moho topography reaches a minimum value to the southwest of the study area and a maximum depth to the NNE. So far, quite a few previous studies have addressed receiver function analysis for Southern Norway (Kanestrøm, 1973; Kosarev et al., 1987; Ottemöller & Midzi, 2003; Svenningsen et al., 2007; Kolstrup & Maupin, 2013; Frasetto & Thybo, 2013). Ottemöller & Midzi (2003) identify a crustal thickness between 34 – 36 km depth for the NAO01 station, as well as Kolstrup & Maupin (2013), who calculated a thickness of 34 km. In the same way, Kanestrøm (1973)

17

and Svenningsen et al. (2007) obtained a Moho depth of 32 km. From this study, we obtained 33.5 km for the same station, which is in a good agreement compared with the other authors. Additionally, the obtained Moho depth for NC303 and NC405 according to Svenningsen et al. (2007) is 38 and 39 km, respectively, very well coinciding with the 38.4±0.31 and 37.8±0.67 km obtained using our approach. Lastly, Kolstrup & Maupin (2013) found a crustal thickness of 39 km for NC204 and 38 km for NC602, once again in good agreement with our results, even considering a difference of ~2 km in the NC602 result. To better visualize these results, the Hκ contour plots are presented (Figure 6). The optimum solution over the H vs Vp/Vs space is in general well defined for all seismic stations. Particularly, NC405 and NC602 are presenting the most spread solution, however, its identification still remains clear (Table 3 & Figure 6)

**Table 3: Hκ Stacking results per station, including projected errors. The western cluster is shown in orange and the eastern one in blue.**

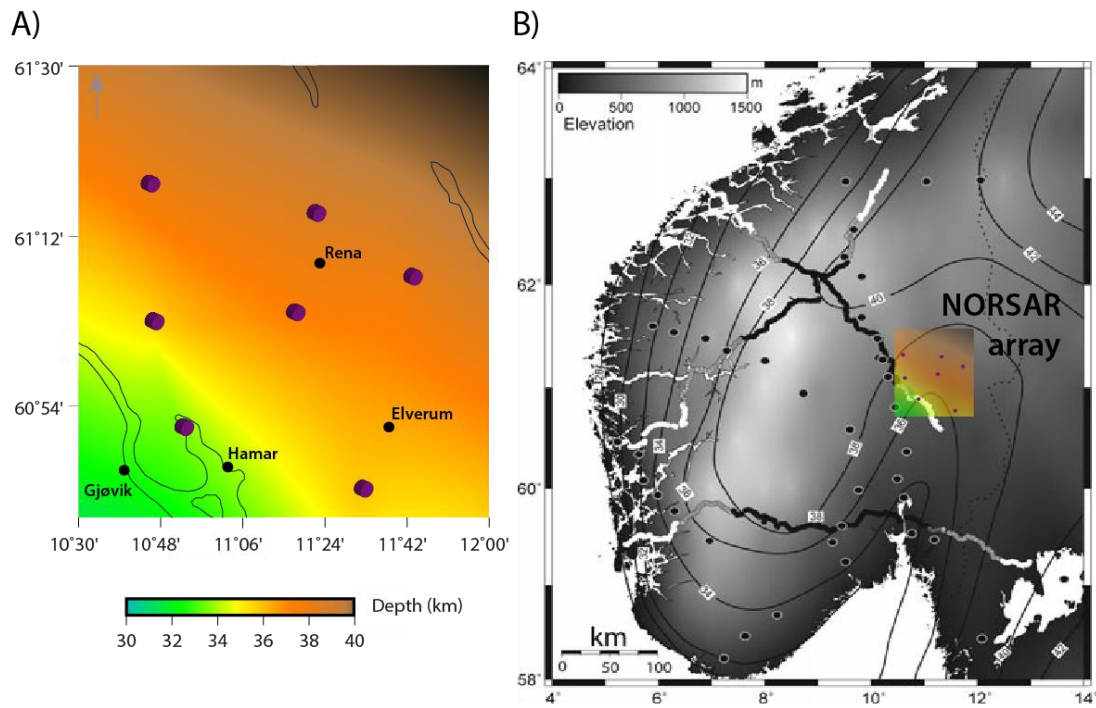| Station | H (km) ± | κ± | Poisson's ratio |
|---|---|---|---|
| NAO01 | 33.5 ± 0.31 | 1.72 ± 0.015 | 0.245 |
| NBO00 | 35.3 ± 0.30 | 1.71 ± 0.02 | 0.240 |
| NC204 | 37.8 ± 0.31 | 1.76 ± 0.015 | 0.262 |
| NC602 | 35.9 ± 0.40 | 1.78 ± 0.05 | 0.269 |
| NB201 | 37.1 ± 0.31 | 1.73 ± 0.01 | 0.249 |
| NC405 | 37.8 ± 0.67 | 1.79 ± 0.09 | 0.273 |
| NC303 | 38.4 ± 0.31 | 1.71 ± 0.02 | 0.240 |

*Figure 5. **A.** Local crustal thickness beneath the NORSAR network. Purple circles correspond to the location of seismic stations. **B.** Original Moho map for Southern Norway proposed by Stratford et el., (2009). The original image was modified overlapping the results obtained in this research for comparison purposes.*
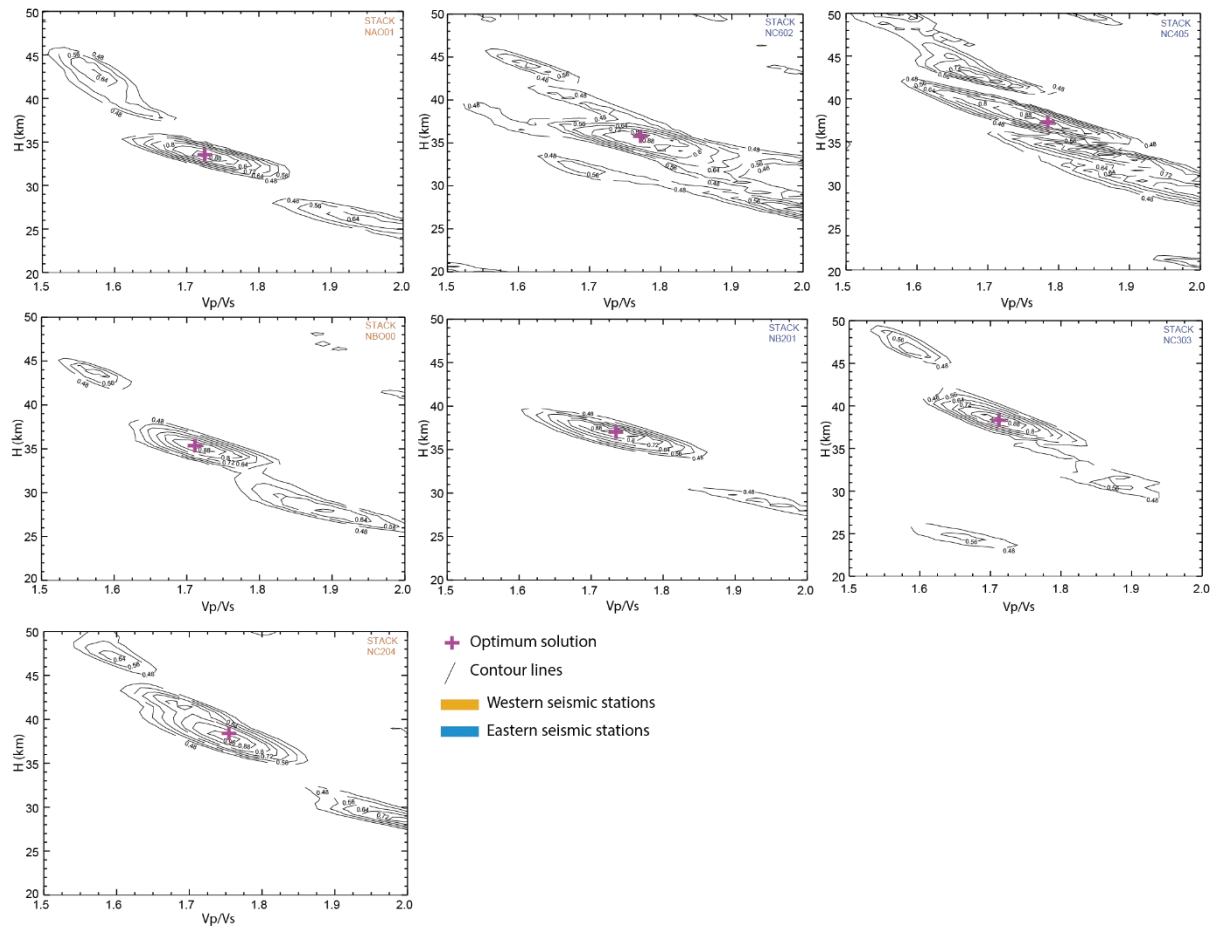
*Figure 6: HK stacking results for the seven stations. Pink cross is showing the optimum solution of H and Vp/Vs, determined by stacking analysis and using a reference velocity of Vp = 6.2 km/s. The contour lines are spaced at intervals of 0.08.*

Table 3 additionally lists the obtained Vp/Vs ratios for each station. It is important to note that these values correspond to an average estimation of the bulk properties for the entire crust (Zhu & Kanamori, 2000). Hence, the results will be affected by the rock elastic properties just if the layer thickness or certain composition comprises a substantial part of the crust. Unfortunately, for our small study area there are no available models that explain in detail the thickness of all observed geological units. To overcome this issue, we will use segments of regional models (Stratford & Thybo, 2011; Ebbing et al., 2012) to try to explain the obtained results.

The highest values were found to the easternmost part of the study area, particularly under the stations NC405 and NC602. Under normal conditions with respect to pressure and fluid presence, the latter could be related to the granitic-dioritic composition of the bedrock that is prevailing in the zone (Figure 4), which thickness is reaching approximately14 km according to the model proposed by Ebbing et al. (2012). Furthermore, focusing on the crustal composition average, the small gabbro intrusions in the area, together with the flank of a mushroom-shaped gabbro body detected at above 5 km depth, plus an intrusive magmatic body at around 18 km depth close to the NC602 station (Ruud & Husebye, 1991),

may indicate an additional reason for an increased crustal density. A similar range of Vp/Vs values between 1.74 and 1.84 has been cited by Holbrook et al. (1992) for granite, granodiorite and gabbroic rocks.

Intermediate values (1.71 – 1.73) were found for the seismic stations NAO01, NBO00, NB201 and NC303, mainly affected by the existing sedimentary layers (Figure 4), which reach a thickness from 5 to 7 km (Ebbing et al., 2012; Stratford & Thybo, 2011). The Vp/Vs value under the NC204 station corresponds to a particular case, where we could observe a relatively high value equal to 1.76. According to Domenico (1984), this ratio is the maximum that can be reached for consolidated sedimentary rocks (1.59 < Vp/Vs < 1.76). Its high value, compared with the surrounding stations, is reasonable considering the location of the station in the central part of the Åsta basin (Figure 4). In this case, according to previous research, the basin is reaching a maximum thickness of 4 km (Nystuen, 1981; Skilbrei et al., 2002; Olesen et al., 2007; Bjørlykke & Olesen, 2018), enough to influence the average Vp/Vs value.

## 4.2. Poisson's ratios and the current lithological configuration
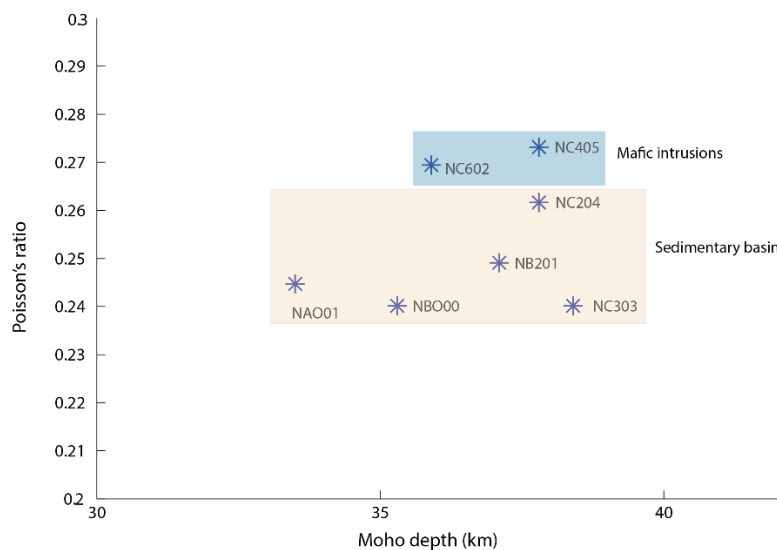


*Figure 7: Poisson's ratios vs Moho depth for all seismic stations. Blue and orange boxes are grouping the different lithological compositions to the west and east of the study area.*

The elastic parameters could be used as well to interpret how the geological context configured the current rock composition of the crust beneath the seismic stations and the adjacent areas. Tectonic regimes related to Paleozoic orogenic belts are exhibiting in general felsic to intermediate crustal compositions (~0.27±0.03 of median and average) and a crustal thickness of ~33.4±5.6 km depth (Zandt & Ammon, 1995). In the case of the Hedmarken area, the averages are ~0.25 and 36.54, for the Poisson's

ratio and the Moho depth, respectively, showing that the zone is currently fundamentally influenced by the Caledonian orogeny during the Silurian. This average Poisson's ratio is additionally in accordance with previous results obtained by Stratford & Thybo (2011a).

The highest Poisson's ratios (~0.275) are located to the east of the study area, under stations NC405 and NC602 (Figure 7). We hypothesize that these values are influenced by the mafic intrusions (Ruud & Husebye, 1991), mainly gabbro bodies and dolerites (Söderlund et al., 2005, 2006) (Figure 4) of Middle to Late Proterozoic age, and related to the pre-Sveconorwegian interval as well as the Sveconorwegian orogeny (Figure 1A). As the average Poisson's ratio for southern Norway is around 0.25, the value is normally interpreted as a lack of a significant mafic lower crust (Stratford & Thybo, 2011a). In this sense, the intrusions in the Hedmarken area could be the main reason for the Poisson's parameter increase.

The mafic signature is present all over the zone following the northwestern orientation of the TIB (Figure 1 & Figure 4). However, for the stations located on the Åsta basin and its borders the Poisson's ratios are lower (0.24 -0.26). This could be in accordance with the presence of Late Precambrian to Middle Ordovician sedimentary layers on top of the TIB and posterior intrusions, which have mainly a felsic signature which is decreasing the crustal average of the Poisson's values (Figure 7). According to Bjørlykke & Olesen (2018), these sedimentary layers could correspond to the Lower and Middle Caledonian nappe units mostly composed by meta-sediments and basement rocks from Baltica.

According to the obtained Poisson's ratios (Table 3 & Figure 7), we estimate the percentage of silica content (%SiO$_2$) using the average crustal measurements from Stratford & Thybo (2008a). As for crustal rocks in southern Norway the silica percentage exceeds 55% (Figure 8A), we will use the relation proposed by Christensen (1996) (Equation 4), for the calculation:

$$\%\mathrm{SiO}_2 = 100.9 - 496\sigma^2 \qquad\qquad (6)$$

As is expected according to the previous results, the silica content decreases to the east of the area reaching the minimum values ranging between 64% to 65%. According to this and the lack of a mafic lower crust, we estimate that the percentage of mafic intrusions can reach ~35% (Figure 8B).
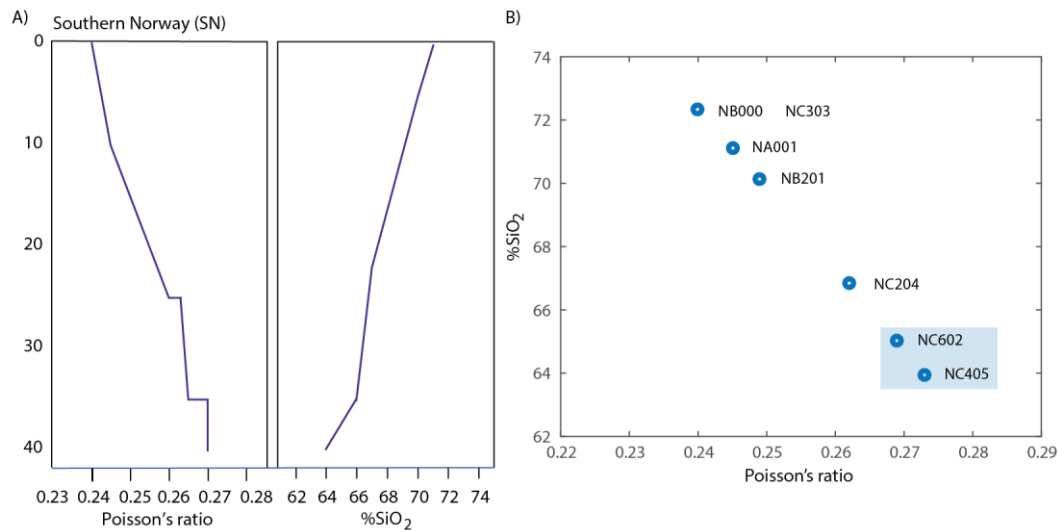
*Figure 8: A) Poisson's ratios and silica content (%SiO2) curves for southern Norway (data and image from Stratford & Thybo, 2011a) B) Poisson's ratio vs. percentage of silica content (%SiO2). The lowest percentages are boxed in blue.*

The compositional signature detected previously by analyzing the Vp/Vs and Poisson's ratios, can be clearly observed in the magnetic anomaly map (Olesen et al., 2010c), where high magnetic anomalies related to the previously described gabbro bodies (Figure 4)  appear directly connected to the location of the easternmost stations NC405 and NC602 (Figure 9). Meanwhile, to the west of the study area, low magnetic anomalies can be linked to the stations on and around the Åsta basin, establishing a correlation between low Poisson's ratios and the presence of a thick-felsic composition sedimentary basin which would be covering the mafic traces (Figure 9).
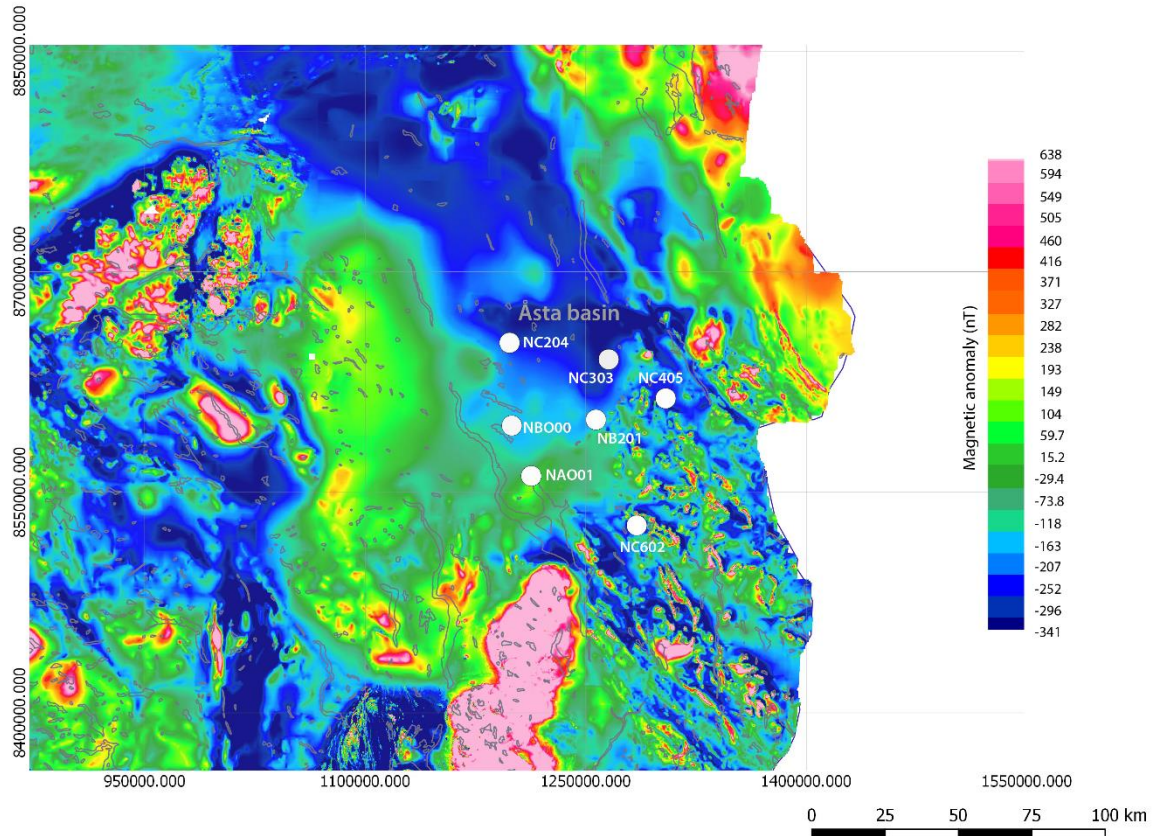
*Figure 9: Magnetic anomaly map cropped for the study area. The white dots are showing the NORSAR seismic stations and the location of the Åsta basin is marked. The high-frequency anomalies at to the stations NC405 and NC602 and farther southeast represent mostly outcropping metagabbros.*

### 4.3. 1D velocity model

The resulting mean S-wave 1D profiles are shown in Figure 10 for all seismic stations. In these curves, the layer boundaries as well as the Vs values in each layer were set by the model, according to the input parameters (Table 2). Three different models were tested in order to observe geological features at different scales. The model space for model 3 can be observed in the Appendix 2 (Figure S3). The first model was considered using 35 layers as maximum (Figure 10). One of the main problems that arise using this number of layers was the poor resolution of the Moho depth, possible influenced by the layer thickness, which smooth the velocity interfaces. However, shallow intracrustal discontinuities can be easily identified, for example, in receiver functions and velocity models related to the Åsta basin (stations NAO01, NC204, NBO00 and NC303 in Figure 3 & Figure 10). The second model was considering 15 layers as maximum (dotted lines in Figure 10). As is expected, the transition related with the Moho depth is better defined. The last model was done with 5 layers as maximum. In this case, only the largest transitions can be observed, and the discontinuity related with the Moho depth is fitting well with the previous models (Figure 10). All the models are producing very similar velocity ranges and transitions, which is a good sign of the model steadiness.

24

One of the main features that is observed in the mean velocity model in relation to the western cluster, corresponds to a low-velocity zone at c. 0 – 7 km depth. Several physical features can be linked with an anomalous velocity layer: temperature, density, saturation, fractures, confining and pore pressure, fluid content and stress-induced velocity anisotropies (among others; O'Connell & Budiansky, 1974; Batzle & Wang, 1992; Holbrook et al., 1992; Christensen & Mooney, 1995; Brocher, 2005; Vega et al., 2006; Wang et al., 2009; Jaya et al., 2010). However, considering the sedimentary lithology that was previously discussed, density variations are the most probable factor that is influencing this behavior.
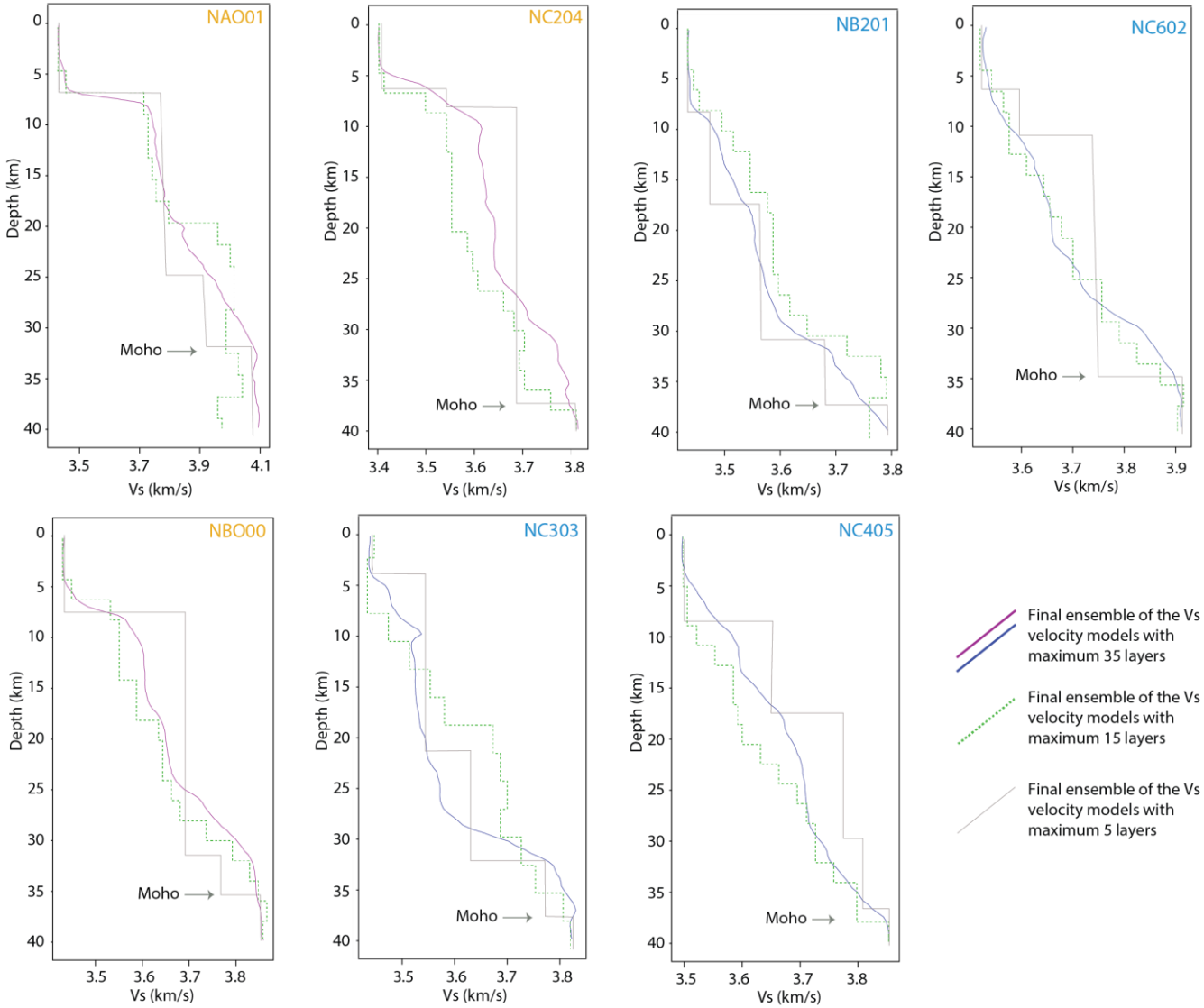


*Figure 10: Posterior ensemble showing the 1D S- wave velocity model for all stations. The seismic stations belonging to the western cluster are shown with an orange legend. Seismic stations corresponding to the eastern part, are shown with a light blue legend.*

## 4.4. 2D/3D density models

Receiver function analysis techniques do not allow detailed interpretations of small crustal features (Hayes & Furlong, 2007). However, more elaborated examinations can be done by connecting them with other geophysical methods. For example, given the relationship between seismic velocities and density, the gravity measurements are commonly incorporated to the analysis in order to better understand and interpret local geology (Lees & Vandecar, 1991). In this way, the intra-crustal discontinuities observed in the receiver function waveforms and the velocity models can be validated by forward gravity modelling.

To better visualize geological features related to the abovementioned low-velocity layer (Figure 10), a 2D density model was generated through our 35 layers velocity model (Figure 11). This selection allows us to observe even small velocity variations and therefore to have a better visualization of detailed crustal features. Considering the large network aperture (~100 km), this model attempts to define general features about local geology in horizontal and vertical sections. Density values were calculated applying the Nafe–Drake relationship (Ludwig et al., 1970), using the crustal ratio κ to obtain $Vp$.

Horizontal sections indicate the prevalence of the anomalous layer approximately until 6.2 km depth, where the density increase its values (Figure 11). To the northwest of the study area, low densities are characterizing the zone, which are mainly related to the Åsta basin area. To the south and northeast, the density increases according to lithology (Figure 4), reflecting well the granitic compositions and the presence of the mafic intrusives.
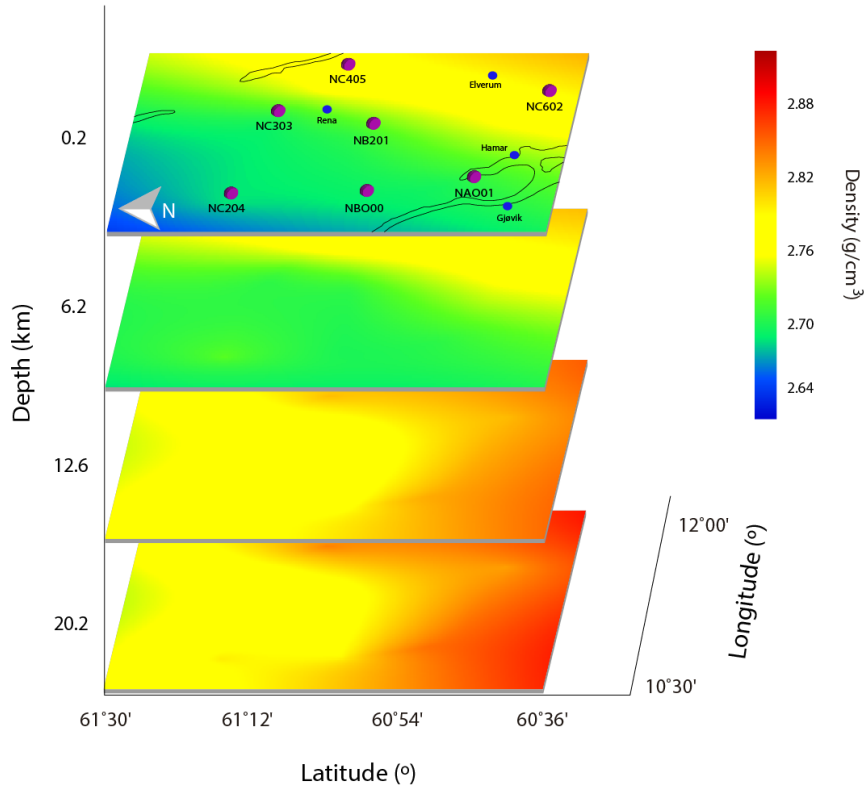
*Figure 11: Horizontal projections for the density model until 20.2 km depth. Seismic stations in purple circles, main cities and contours are projected above the shallow layer.*

With respect to the vertical sections, three profiles were analyzed until 20 km depth: AA' and AA'', both crossing the Åsta basin in NS and EW directions, respectively, and BB', crossing the easternmost part of the study area in NS direction (Figure 4). As can be seen in the AA' profile, the observed gravity is increasing from north to south (Figure 12A & Figure 13A), which is in good correlation with the calculated density distribution along this model, and which gives insights about the thickness of the different geological units. The low-density layer in the north coincides well with the location of the Åsta basin (Figure 4), constituted of up to c. 1.5 km thick meta-sandstones in the Uppermost and Upper Caledonian Allochthon units (Figure 12A). The thickness of the nappes and consequently of the basin was previously estimated to a maximum of c. 5 km (Nystuen, 1981; Skilbrei et al., 2002; Olesen et al., 2007). However, from the present results we are proposing a separation between the sediments and the Precambrian basement domains (indicated in Figure 12A) with a sediment – basement transition at up to 6.0 to 6.5 km depth that can observable in the north of the section. Southwards, the basin is becoming shallower and is pinching out, where is onlapping on denser Precambrian basement coinciding with previous structural models (Bjørlykke & Olesen, 2018).

According to this density distribution, it is possible to infer most likely NW dipping ENE-WSW striking major normal faults in the Precambrian basement, which mark the tectonic boundary of the basin. The faults are consistent on profiles AA' and AA'', where a similar setting is observed (Figure 12B). However, the profile is along a gravity slope with a predominant gravity high south of the profile, correlating with exposed Precambrian bedrock and two local gravity lows, separated by a Precambrian basement ridge (Figure 4 & Figure 13A) to the north. Considering the large aperture of the seismic array, the complex and rapid sequences of Caledonian nappes and Precambrian basement are beyond the resolution of the derived density model, which is why only the major units correlate with the observed gravity. Furthermore, both profiles exhibit an evident dip angle to the north, which is taking values between 20°–30° similar to what was proposed by Bjørlykke & Olesen (2018).

A third N-S striking profile BB' is situated to the east of the survey area and almost entirely in the Precambrian bedrock domain (Figure 12C). The densities are significantly higher and the Bouguer gravity variation more constant (max. 16 mGal). However, the profile indicates nicely the segmentation and faulting of the Precambrian basement in this region with apparently horst structures and SSW dipping faults (see fault 'b' in Figure 12C), also reflected in the gravity data. The density contrasts and the inferred deep faults must be considered as a reliable proof that the Åsta basin and the Sparagmite basins in general are tectonically controlled along a crustal scale NW- SE striking weakness zone, which continues south of the Sparagmite basins and furthermore is noticeable sub-parallel and in extension to the Jan Mayen Fracture Zone to the north.

An extra feature regarding the BB' profile arise considering the gabbro intrusions located in the area. Ruud & Husebye (1991) proposed the existence of a weak reflector at a depth of 18 km beneath the NORESS seismic array. However, considering its small aperture (~3 km), the resolution was probably poor to locate a six times greater depth anomaly. In the same way, Christofferson et al. (1988), found a conversion boundary at about 18 km depth using SV-wavelets data. Our BB' cross section shows to its southern end a deep high-density anomaly (~15 km; $\rho$ >2.85 g/cm$^3$) (Figure 12C), which could correspond to the cited magmatic body. This structure seems to agree with the lithology and location proposed by the abovementioned authors.
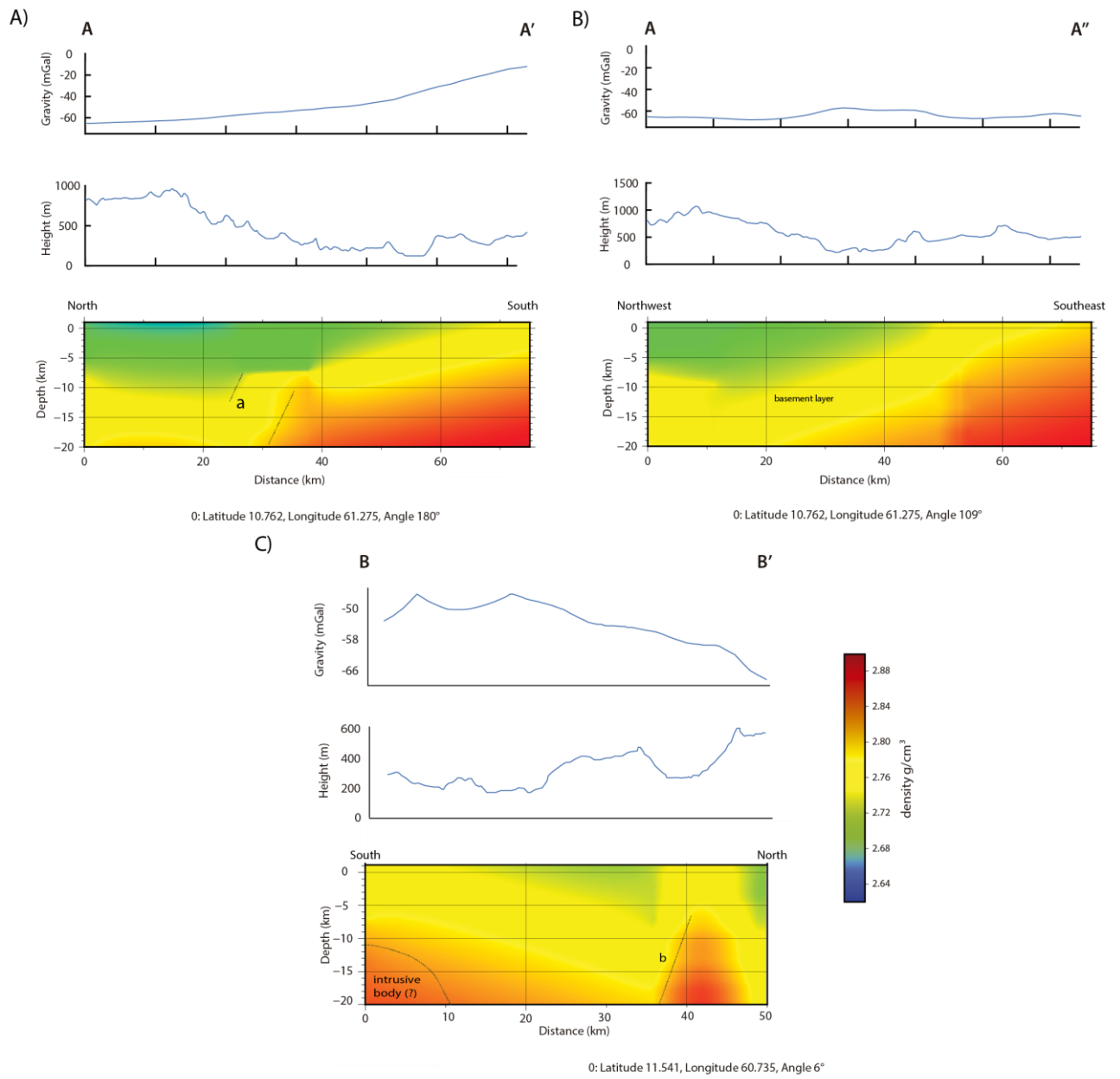
*Figure 12: A,B & C correspond to the density models for the AA', AA'' and BB' cross sections. Additionally, topography and observed gravity are shown. Inferred thrust faults are marked with dotted lines. All profiles are using the same color palette.*
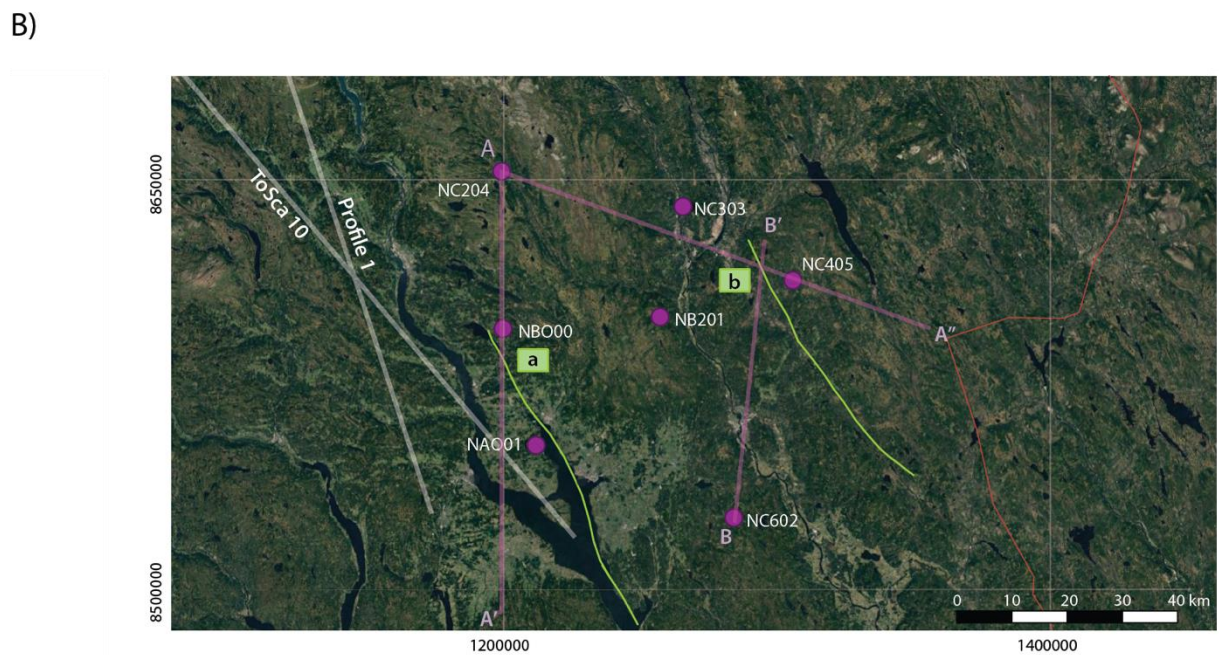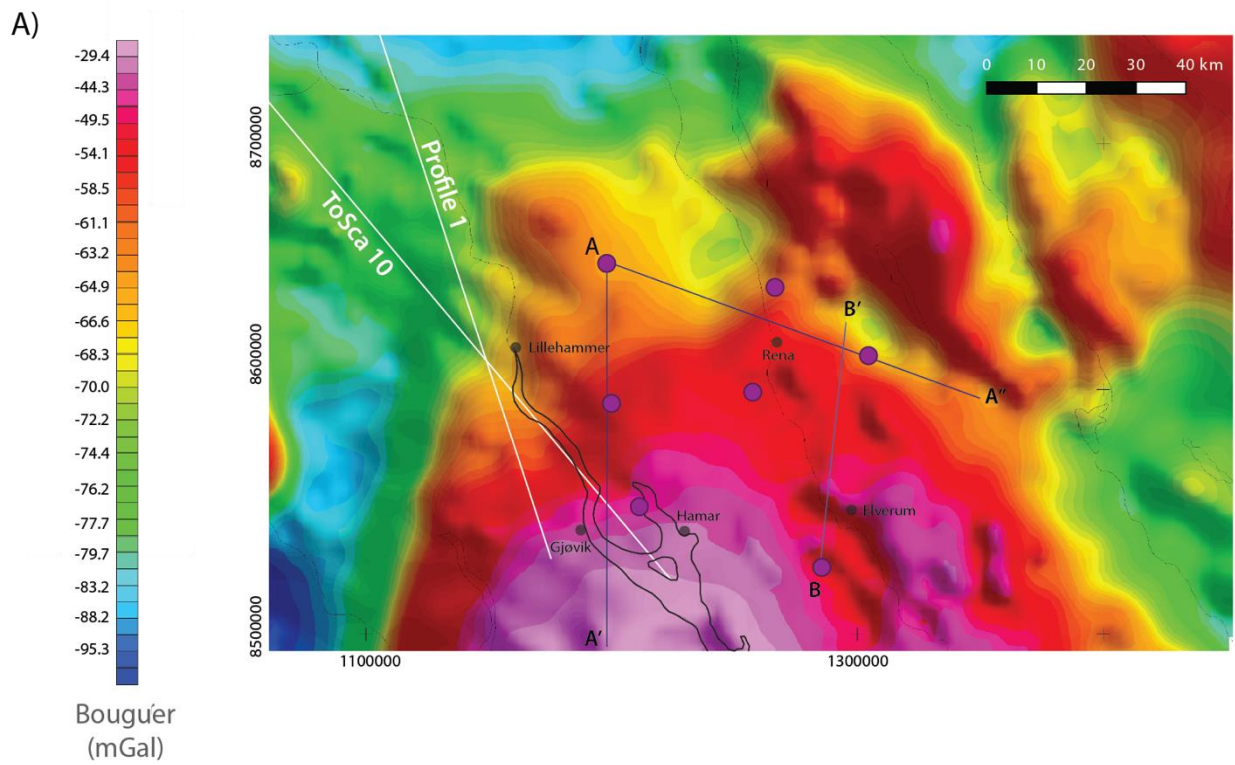
*Figure 13: A. Bouguer gravity map (Olesen et al., 2007) with seismic stations. Profiles in the present paper are shown with a continuous black line. Structural cross section (Profile 1) from Bjørlykke & Olesen, (2018) and MT profile (ToSca'10) from Cherevatova et al., (2014) are shown with a continuous white line. B. Local map showing seismic stations and profiles, marked with coarse pink lines. Structural cross section and MT profile are also shown. The identifiable fault observed in the AA' profile is shown in green; profile and fault intersection points are marked with green squares.*

To support our interpretation regarding the observed gravity along the Åsta basin, we constructed a simplified 2D forward modelling (Figure 14). From this exercise, where we applied a 3-layer model with constant densities, observed and calculated gravity are in good agreement. Remaining misfits are small due to the applied simplification, but in general the modelling is supporting the validity of the proposed density model and the geometry and thickness of the basin and the Caledonian and Precambrian basement units.



Figure 14: Forward gravity model along the AA' profile. (Top) Dotted green line corresponds to the observed gravity. Continuous pink line corresponds to the model. (Bottom) Density model including the modeling points in red.

## 4.5. Comparison with previous models
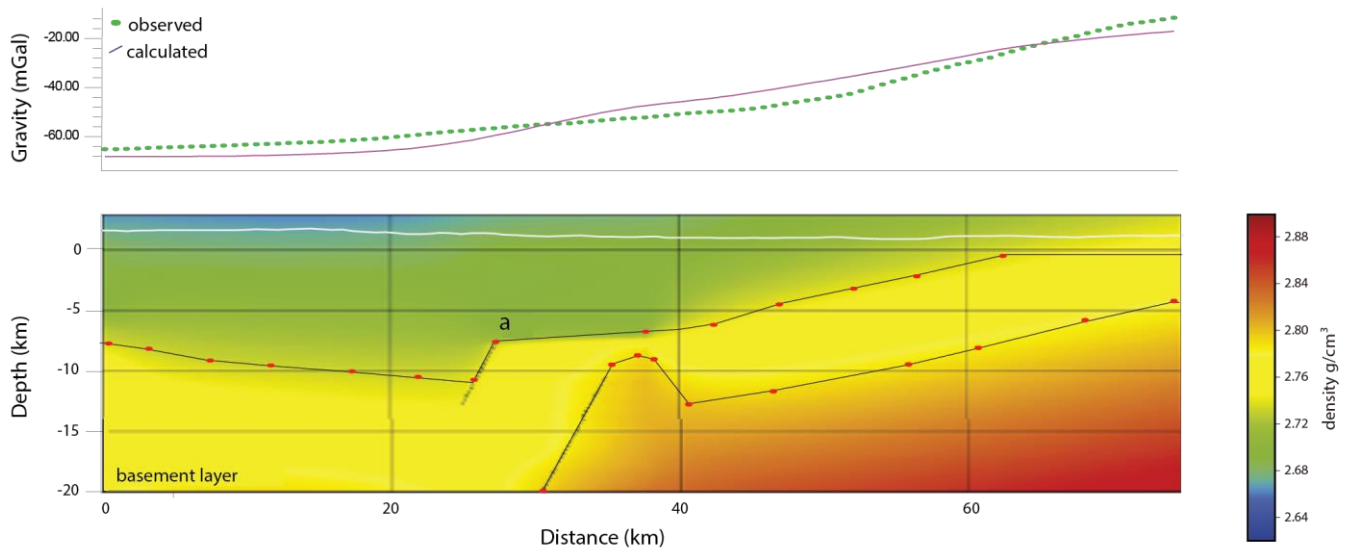
To draw a comparison between the density model and geological features, we are establishing a cross-correlation with two models recently developed in the area. The first one corresponds to a geological cross-section model proposed by Bjørlykke & Olesen (2018) (Figure 15), and the second one with a two-dimensional inversion model from magnetotelluric data presented by Cherevatova et al. (2014) (Figure 16). Both models correspond to regional studies, hence for our analysis we are just considering those subsections spatially correlated with our study area (see locations of Profile 1 & ToSca'10 lines in Figure 15A & Figure 16A).

Overlapping the last 75 km of the geological cross section of Bjørlykke & Olesen (2018), with our density model, a clear correlation regarding structures and geological units can be observed (Figure 15A & 15B). According to the density model, autochthonous Precambrian basement (Figure 15A) would reach densities above 2.72 g/cm$^3$, being related with Domain number 3 (in yellow in Figure 15B). Meanwhile, the sedimentary strata and the Caledonian nappe system exhibit lower densities between 2.62–2.71 g/cm$^3$. In agreement with this, Domain 1 (blue) would be equivalent with the Upper &

Uppermost Caledonian nappe units, while Domain 2 (green) would be related to the Lower & Middle nappe units plus meta-sediments (Figures 15A & 15B). In addition, the south vergency that can be observed in the density model would be mainly related with the thrusting process above the Mesoproterozoic basement.

As was abovementioned, there is an evident dip angle to the north observed in the density model which is taking values between 20°–30° (Figure 12A). Seemingly, this behavior is replicated to the south-east of the Åsta basin (see profile AA'' in Figure 12B). To check this assumption, a 3D model was developed (Figure 12C). The green iso-surface shows the outline shape of the Åsta basin according to the density model, where the configuration of the basin supports the dip angle to the north and to the east of the study area. Furthermore, the obtained contour allows us to delimit the maximum depth of the basin in 6.6 km, approximately 1.6 km deeper with respect to previous models (Nystuen, 1981; Skilbrei et al., 2002; Olesen et al., 2007; Bjørlykke & Olesen, 2018).

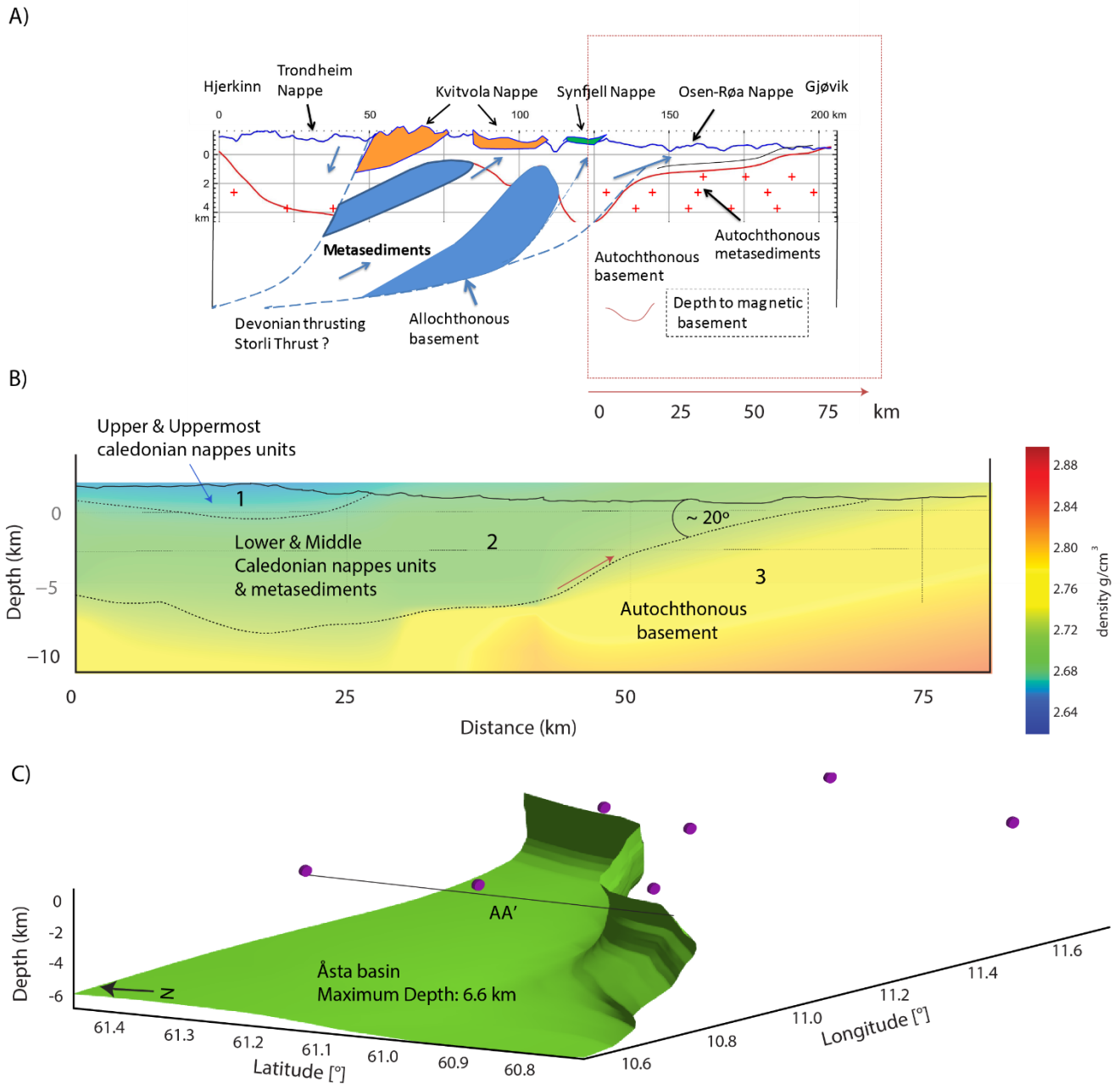*Figure 15. Geological cross section presented by Bjørlykke & Olesen (2018). Red dotted box is showing the subsection where the profile is compared with the AA' density model. **B.** Density model for the AA' cross section, including the interpretation according to (a). **C.** 3D model showing the outline shape of the Åsta basin. Purple dots correspond to the seismic network and the AA' profile is shown with a continuous black line.*
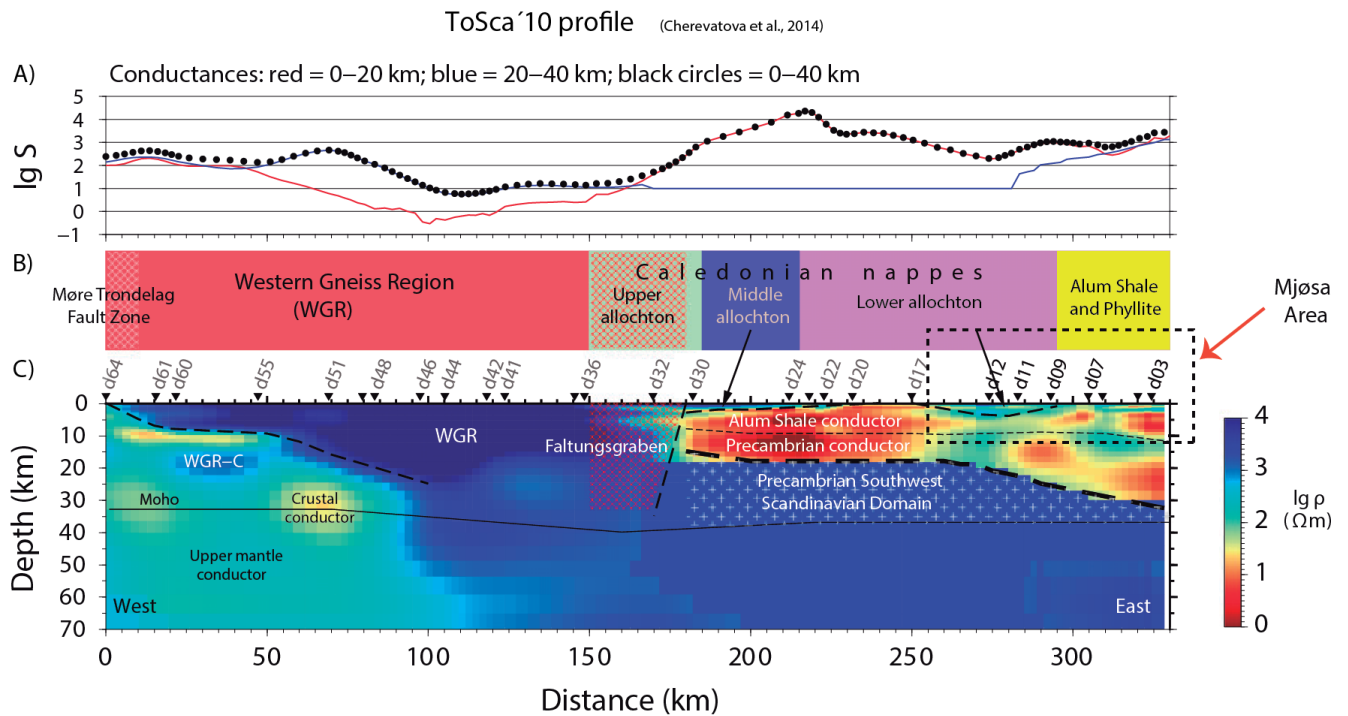
*Figure 16: Crustal conductivity and interpretation along the ToSca'10 profile (see Figure 10 in Cherevatova et al. (2014) and location in Figures 1, 6 & 10). This figure was modified showing the study area that is analyzed in this paper. Black and dotted box corresponds to the segment equivalent to Mjøsa.*

On the other hand, the MT profile ToSca'10 is crossing the Scandinavian orogen in southern Norway following a southeast direction, and its last part coincide with the Mjøsa area to the south of the NORSAR array (Figure 16A). Their calculation of the crustal conductance was made for three depth ranges (Figure 16A), the surface geology can be observed in Figure 16B, and the interpretation model is in Figure 16C. Just the easternmost part of the ToSca'10 profile was considered for our analysis, for which we are taking the last BMT sites with a total extension of around 100 km long. As can be observed in the study area (dotted black box in Figure 16C) a high resistivity zone is followed by a low-resistivity layer to the east. Comparing the MT model with the AA' profile and the structural cross section (Figures 12A & 15A, B), the presence of sediments, including sandstones and conglomerates to the north, arise as an explanation for this point (Figure 4). According to our density-structural model, this high resistivity layer would be related with Neoproterozoic to Cambro-Ordovician metasediments belonging to the Lower and Middle Caledonian nappes units (Figure 15B). Same geometry, depth and dip can be observed in both models, as well as Cherevatova et al. (2014) interpret this zone as part of the Lower Allochthon. In the same way, the high conductivity shales to the southeast agree with the southernmost end of the AA' profile (Figure 12A). Regarding the model in Figure 16B, it can also be speculated that this low resistivity zone corresponds to so called Precambrian conductor, which was tectonically exposed and is being part of the uppermost basement. The last could be additionally supported regarding the basement depth line above discussed.

34

# 5. CONCLUSIONS

A receiver function analysis using teleseismic waveforms obtained from the three-component NORSAR array was developed in the Hedmark area. Well-defined peaks for the arrival of the Ps phase suggest a clear Mohorovicic discontinuity between 3.5 and 5 s, with an increasing in the arrival times that is notable to the northeast. At the same time, intracrustal reverberations observed before the Moho Ps phase arrivals were linked to shallow structures corresponding to the upper crust beneath the array. According to the local geology, these reverberations could correspond to thick sedimentary layers related to the Åsta basin, estimated in previous research to be about 4 km deep (Nystuen, 1981; Skilbrei et al., 2002; Olesen et al., 2007; Bjørlykke & Olesen, 2018). So far, receiver functions studies were not capable to distinguish such geological features as the characterization of small and local structures was not the main goal in any of those research. In this sense, our study present new insights that help to understand the evolution of the upper crust in the area.

The receiver functions were used in addition to obtain the local Moho depth, the Vp/Vs parameter and the Poisson's ratio using the $H$K - stacking method. The results show a good correlation with the local surface geology, as well as the values support the presence of mafic intrusions that have been identified at the zone using other geophysical methods (Ruud & Husebye, 1991). Particularly, the Poisson's ratio is well correlated with the average crustal composition of felsic to intermediate rocks. The compositional differences that can be deducted from our results can also be noticed and correlated with the magnetic anomalies: high anomalies could be found under the easternmost seismic stations meanwhile low magnetic anomalies were found in connection with the Åsta basin. In this respect, we not only confirm former studies developed in the area, but also we improve the general understanding adding new details to the overall picture.

The 1D S-wave velocity model obtained through the transdimensional inversion reflects clearly the two main discontinuities above discussed. The Mohorovicic discontinuity is patent in our 15- and 5-layers model (Figure 10) and the low velocity- low density layer is well identified to the north-west of the study area. Correlating the density model with an available structural cross-section, this layer was linked to sediments and meta-sediments that lie above the Mesoproterozoic basement and which are spatially correlated with the Åsta basin. With this respect, the receiver function analysis developed in the area was in addition useful to demarcate the shape and depth of sedimentary layers, as it has been observed before in other studies (Fontaine et al., 2015; Rindraharisaona et al., 2017). This constitutes a new example to corroborate the method in finding intra-crustal discontinuities with density or elastic anomalies. The observed discontinuities alongside density and gravity modelling allow us to infer the presence of major faults which would be related with the basement – sediments transition zone in the Åsta basin.

With this model we give more geological and geophysical details in an area that has been studied regionally many times. Including the present research, just a few models describe small and local areas in southern Norway (see references above). Even considering the difference between the scales, our model is agreeing very well with previous studies related to regional receiver functions analysis, geological concepts derived from surface geological studies and the estimation of the Moho depth and related parameters.

## 7.  REFERENCES

Ammon, C.J., Randall, G.E., Zandt, G. 1990: On the non-uniqueness of receiver function inversions, J. Geophys. Res., 95, 15303–15318.

Ammon, C.J. 1991: The isolation of receiver effects from teleseismic P waveforms, Bull. Seism. Soc. Am. 81, 2504–2510.

Batzle, M. & Wang, Z. 1992: Seismic properties on pore fluids. Geophysics. 57. 1396–1408.

Bayes, T. 1763. An essay towards solving a problem in the doctrine of chances. Phil. Trans. R. Soc. Lond. 53. 370-418. (Reprinted by Barnard, G.A. 1958. Biometrika 45. 293-315).

Bingen, B., Andersson, J., Söderlund, U., Möller, C. 2008a: The mesoproterozoic in the Nordic countries. Episodes 31 (1), 29–34.

Bjørlykke, A. & Olesen, O. 2018: Caledonian deformation of the Precambrian basement in southeastern Norway. Norwegian Journal of Geology 98, 1–16.

Bodin, T., Sambridge, M., Tkalčić, H., Arroucau, P., Gallagher, K. & Rawlinson, N. 2012: Transdimensional inversion of receiver functions and surface wave dispersion. J. Geophys. Res., 117, B02301. doi:10.1029/2011JB008560.

Brocher, T.M. 2005: Empirical relations between elastic wavespeeds and density in the earth's crust. Bulletin of the Seismological Society of America. 95. No 6. 2081–2092.

Cherevatova, M., Smirnov, M., Korja, T., Kaikkonen, P., Pedersen, L.B., Hübert, J. 2014: Crustal structure beneath southern Norway imaged by magnetotellurics. Tectonophysics 628, 55–70.

Christensen, N.I. & Mooney, W.D. 1995: Seismic velocity structure and composition of the continental crust: A global view. Journal of Geophysical Research. 100. 9761–9788.

Christensen, N.I. 1996. Poisson's ratio and crustal seismology. Journal of Geophysical Research 101. 3139-3156.

Christofferson, A., Husebye. E.S. & Ingate, S.F. 1988: Wavefield decomposition using ML probabilities in modelling single site 3 component records. Geophys. J. 93. 197–213.

Clayton, R.W., Wiggins, R.A. 1976: Source shape estimation and deconvolution of teleseismic body waves. Geophys. J. R. astr. Soc. 47. 151–177.

Denison, D. G. T., Holmes, C.C., Mallick, B. K., Smith, A. F. M. 2002: Bayesian Methods for Nonlinear Classification and Regression, Wiley, Chichester.

Domenico, S.N. 1984: Rock lithology and porosity determination from shear and compressional wave velocity. Geophysics 49 (8), 1188e1195.

Ebbing, J., England, R.W., Korja, T., Lauritsen, T., Olesen, O., Stratford, W., Weidle, C. 2012: Structure of the Scandes lithosphere from surface to depth. Tectonophysics. 536–537. 1–24.

Fontaine, F., Barruol, G., Tkalcic, H., Wölbern, I., Rümpker, G., Bodin, T., Haugmard, M. 2015: Crustal and uppermost mantle structure variation beneath La Reúnion hotspot track. Geophysic Journal International. 203. 107–126.

Frasetto, A. & Thybo, H. 2013. Receiver function analysis of the crust and uppermantle in Fennoscandia- isostatic implications. Earth and Planetary Science Letters 381. 234-246.

Gabrielsen, R.H., Nystuen, J.P. & Olesen, O. 2018: Fault distribution in the Precambrian basement of South Norway. Journal of Structural Geology. 108. 269–289.

Gallagher, K., Charvin, K., Nielsen, S., Sambridge, M., Stephenson, J. 2009: Markov chain Monte Carlo (MCMC) sampling method to determine optimal models, model resolution and model choice for Earth Science problems. Mar. Pet. Geol. 26. 525–535.

Gallagher, K., Bodin, T., Sambridge, M., Weiss, D., Kylander, M., Large, D. 2011: Inference of abrupt changes in noisy geochemical records using Bayesian transdimensional changepoint models, *Earth and Planet. Sci. Lett.*, 311, 182–194. doi:10.1016/j.epsl.2011.09.015

Geological map of Norway (scale 1:250.000). https://www.ngu.no/emne/datasett-og-nedlasting

Grad, M. & Tiira, T. 2009: ESC Working Group. The Moho depth map of the European plate. Geophys. J. Int. 176. 279–292.

Green, P. 1995: Reversible Jump MCMC computation and Bayesian model selection. Biometrika. 82. 711–732.

Green, P. 2003: Transdimensional Markov chain Monte Carlo. Highly Struct. Stochastic Syst. 27. 179–198.

Hayes, G.P. & Furlong, K.P. 2007: Abrupt changes in crustal structure beneath the Coast Ranges of northern California – developing new techniques in receiver function analysis. Geophys. J. Int. 170. 313-336.

Helffrich, G., Wookey, J., Bastow, I. 2013: The Seismic Analysis Code: A Primer and User's Guide. Cambridge University Press, United Kingdom.

Hermann, R. 2013: Computer Programs in Seismology: An evolving tool for instruction and research. Seismological Research Letters 84. 1081–1088.

Holbrook, W.S., Mooney, W.D. & Christensen, N. 1992: The seismic velocity structure of the depth continental crust. Continental Lower Crust. 23. 1–43.

IEarth free software. http://www.iearth.org.au/codes/rj-RF/.

Jaya, M.S., Shapiro, S., Kristindottir, L., Bruhn, D., Milsch, H., Spangenberg, E. 2010: Temperature-dependence of seismic properties in geothermal core samples at in situ reservoir conditions. Proceedings World Geothermal Congress. Bali, Indonesia.

Kanestrøm, R. & Haugland, K. 1971. Profile section 3-4 in Seismic investigations of the crust and upper mantle in Norway, pp. 2-17, ed. Vogel, A., Natural Science Research Council, Stockholm.

Kanestrøm, R. 1973: A crust-mantle model for the NORSAR area. Pure appl. Geophys. 105. 729–740.

Kanestrøm, R & Nedland, S. 1975. Crustal structure of southern Norway: a reinterpretation of the 1965 seismic experiment, Institute report, Seismological Observatory, University of Bergen.

Kinck, J.J., Husebye, E.S. & Larsson, F.R. 1993: The Moho depth distribution in Fennoscandia and the regional tectonic evolution from Archean to Permian times. Precambrian Research 64, 23–51.

Köhler, A., Weidle, C., Maupin, V. 2011. Directionality analysis and Rayleigh wave tomography of ambient noise in southern Norway. Geophysical Journal International 184(1). 287-300.

Köhler, A., Weidle, C., Maupin, V. 2012. Crustal and uppermost mantle structure of southern Norway: results from surface wave analysis of ambient seismic noise and earthquake data. Geophysical Journal international 191(3). 1441-1456.

Kolstrup, M.L., Maupin, V. 2013: A Proterozoic boundary in Southern Norway revealed by joint-inversion of P-receiver functions and surface waves. Precambrian Research. 238. 186-198.

Kosarev, G.L., Makeyeva, L.I. & Vinnik, L.P. 1987: Inversion of teleseismic P wave particle motions for crustal structure in Fennoscandia. Phys Earth Planet. Inter. 47. 11–24.

Lamminen, J., Andersen, T. & Nystuen, J.P. 2015: Provenance and rift basin architecture of the Neoproterozoic Hedmark basin, South Norway inferred from U–Pb ages and Lu–Hf isotopes of conglomerate clasts and detrital zircons. Geol. Mag. 152. 80–105.

Lees, J.M. & VanDecar, J.C. 1991: Seismic tomography constrained by Bouguer gravity anomalies: applications in western Washington. Pageoph. 135.1.

Ligorria, J.P., Ammon, CJ. 1999: Iterative deconvolution and receiver-function estimation. Bulletin of Seismological Society of America 89 (5). 1395–1400.

Lolli, B., Gasperini, P. & Vannucci, G. 2014: Empirical conversion between teleseismic magnitudes (mb and Ms) and moment magnitude (Mw) at the global, Euro – Mediterranean and Italian scale. Geophysical Journal International. 199. 805–828.

Ludwig, W.J., Nafe, J.E. & Drake, C.L. 1970: Seismic Refraction, the Sea. Vol. 4 (Part 1), Wiley-Interscience, New York, 53–84.

Malinverno, A. 2002: Parsimonious Bayesian Markov Chain Monte Carlo inversion in a nonlinear geophysical problem. Geophys. J. Int. 151. 675–688

Möller, C., Andersson, J., Dyck, B., Lundin, I.A. 2015. Exhumation of an eclogite terrane as a hot migmatitic nappe, Sveconorwegian orogen. Lithos, Vol. 226. Pp. 147-168

Mykkeltveit, S. 1980. A seismic profile in southern Norway. Pure appl. Geophys. 118. 1310-1325.

Nystuen, J.P. 1981: The late precambrian sparagmites of southern Norway: a major Caledonian allochthon – the Osen Røa Nappe Complex. American Journal of Science. 281, 69–94.

O'Connell, R. & Budiansky, B. 1974: Seismic velocities in dry and saturated cracked solids. Journal of Geophysical Research. 79, I. 35. 5412–5426.

Olesen, O., Ebbing, J. & Skilbrei, J.S. 2007: Depth to crystalline basement on the Norwegian continental shelf. KONTIKI Final Report, Continental Crust and Heat Generation in 3D. NGU Report. 042, 438 pp.

O. Olesen, M. Brönner, J. Ebbing, J. Gellein, L. Gernigon, J. Koziel, T. Lauritsen, R. Myklebust, M. Sand, D. Solheim, S. Us ov. 2010a. New aeromagnetic and gravity compilations from Norway and adjacent areas — methods and applications. Petroleum Geology Conference series, 7. pp. 559-586

O. Olesen, J. Ebbing, J. Gellein, O. Kihle, R. Myklebust, M. Sand, J.R. Skilbrei, D. Solheim, S. Usov. 2010b. Gravity Anomaly Map, Norway and Adjacent Areas. Geological Survey of Norway.

O. Olesen, J. Gellein, L. Gernigon, O. Kihle, J. Koziel, T. Lauritsen, J.O. Mogaard, R. Myklebust, J.R.Skilbrei, S. Usov. 2010c. Magnetic Anomaly Map, Norway and Adjacent Areas. Geological Survey of Norway.

Ottemöller, L. & Midzi, V. 2003. The crustal structure of Norway from inversion of teleseismic receiver functions. Journal of Seismology 7: 35–48.

Piana-Agostinetti, N. & Malinverno, A. 2010: Receiver function inversion by trans-dimensional Monte Carlo sampling. Geophys. J. Int. 181. 858–872.

Rindraharisaona, E. J., Tilmann, F., Yuan, X., Rümpker, G., Giese, J., Rambolamanana, G., Barruol, G. 2017: Crustal structure of southern Madagascar from receiver functions and ambient noise correlation: Implications for crustal evolution. Journal of Geophysical Research: Solid Earth. 122, 1179–1197.

Roberts, D. & Gee, D.G. 1985: An introduction to the study of the Scandinavian Caledonides. In: Gee, D.G., Sturt, B.A. (Eds.), The Caledonide Orogen – Scandinavia and Related Areas. Wiley & Sons, pp. 485–497.

Roberts, D. 2003: The Scandinavian Caledonides: event chronology, paleogeographic settings and likely modern analogues. Tectonophysics 265, 283–299.

Ruud, B.O. & Husebye, E.S. 1991: Exploring the upper mantle crust: A combined interpretation of 3D imaging and reflection profiling in the NORESS array. Tectonophysics 189, 109–115.

Sambridge, M., Bodin, T., Gallagher, K., Tkalčić, H. 2013: Trans-dimensional inference in the geosciences, *Phil. Trans. R. Soc. A*, 371, 20110547. doi:10.1098/rsta.2011.0547.

Sellevoll, M.A. & Warrick, R.E. 1971. A refraction study of the crustal structure in southern Norway. Bull. Seism. Soc. Am. 61. 457-471.

Skilbrei, J.R., Olesen, O., Osmundsen, P.T., Kihle, O., Aaro, S., Fjellanger, E. 2002: A study of basement structures and onshore-offshore correlations in Central Norway. Norwegian Journal of Geology 82. 263–279.

Srinivas, D., Srinagesh, D., Chadha, R.K., Ravi Kumar, M. 2013. Sedimentary thickness variations in the Indo-Gangetic foredeep from inversion of receiver functions. Bulletin of Seismological Society of America. V. 103. No. 4. 2257-2265.

Söderlund, U, Isachsen, CE, Bylund, G, Heaman, LM, Jonathan Patchett, PJ, Vervoort, JD & Andersson, UB 2005, 'U-Pb baddeleyite ages and Hf, Nd isotope chemistry constraining repeated mafic magmatism in the Fennoscandian Shield from 1.6 to 0.9 Ga', *Contributions to Mineralogy and Petrology*, vol. 150, no. 2, pp. 174-194. https://doi.org/10.1007/s00410-005-0011-1

Söderlund, U., Elming, S-E., Ernst, R.E., Schissel, D. 2006. The Central Scandinavian Dolerite Group – Protracted hotspot activity or back-arc magmatism? Constraints from U-Pb baddeleyite geochronology and Hf isotopic data. Precambrian Research, Vol. 150. Issues 3-4. Pp. 136-152.

Stratford, W., Thybo, H., Faleide, J.I., Olesen, O., Tryggvason, S. 2009: New Moho map for onshore southern Norway. Geophysical Journal International 178, 1755–1765.

Stratford, W. & Thybo, H. 2011a. Crustal structure and composition of the Oslo graben, Norway. Earth and planetary Science Letters 304(3). 431-442.

Stratford, W. & Thybo, H. 2011b. Seismic structure and composition of the crust beneath the southern Scandes, Norway. Tectonophysics 502. 364–382.

Svenningsen, L., Balling, N., Jacobsen, B.H., Kind, R., Wylegalla, K., Schweitzer, J. 2007. Crustal root beneath the highlands of southern Norway resolved by teleseismic receiver functions. Geophys. J. Int. 170. 1129–1138.

Schweitzer, J., Roth, M. 2015. The NORSAR Data Center (FDSN Network Code NO). Biannual report for the FDSN meeting. IUGG General Assembly, Prague, 2015.

Tesauro, M., Kaban, M.K. & Cloetingh, S.A.P.L. 2008: EuCRUST-07: a new reference model for the European crust. Geophysical Research Letters 35, L05313.

Vega, S., Mavko, G., Nur, A., Prasad, M. 2006: Detection of stress induced velocity anisotropy in unconsolidated sands. The Leading Edge. 25. 3. 225–384.

Wang, J., Hung, J. & Dong, J. 2009: Seismic velocity, density, porosity and permeability measured at a deep hole penetrating the Chelungpu fault in central Taiwan. Journal of Asian Earth Sciences. 36, 2–3. 135–145.

Zandt, G. & Ammon, C.J. 1995. Continental crust composition constrained by measurements of crustal Poisson's ratio. Nature. Vol. 374. Pp 152-154.

Zhao, D. 2007: New advances of seismic tomography and its applications to subduction zones and earthquake fault zones: A review. Island Arc. Vol. 10. 1. pp. 68–84.

Zheng, T., Zhao, L., Chen, L. 2005: A detailed receiver function image of the sedimentary structure in the Bohai Bay Basin. Physics of the Earth and Planetary Interiors 152. 129-143.

Zhu, L. & H. Kanamori. 2000: Moho depth variation in southern California from teleseismic receiver functions. Journal of Geophysical Research, **105**, 2969–2980.

## 8. APPENDICES

*Appendix 1: Dimensionality assumption*

Several variations in the receiver functions calculation can be detected due to the moveout. Moveout is describing the changes in the P-S conversion arrival times by variations in the ray parameter of seismic waves of different events (Hayes & Furlong, 2007). This ray parameter is linked to the angle of incidence at which the seismic waves are approaching to the station, so it depends of the distance between the event and the seismometer, as well as the event depth. When several events are being considered, small variations in conversion arrival times are expected (Hayes & Furlong, 2007). To avoid a negative effect of this conversion and therefore destructive stacking of the individual phases, ray parameters must be calculated for each event. In this research, this process was done using the UDTDD script available in the CPS package (Hermann, 2013), which considers hypocentral distances through the GCARC (Great Circle Arc) value and depth. Results are shown in Figure S1. The individual Ps peaks are indicated with a continuous green line to point out the tentative arrival times. In general, they can be clearly observed around 3.5 to 5.0 seconds, as was previously detailed analyzing the stacked receiver function in the main text. As the signals were previously selected by quality and were visually inspected in order to check signal coherence, there are no visible signs of destructive stacking or widening. A similar conclusion can be obtained analyzing arrival times vs back azimuth (Figure S2).
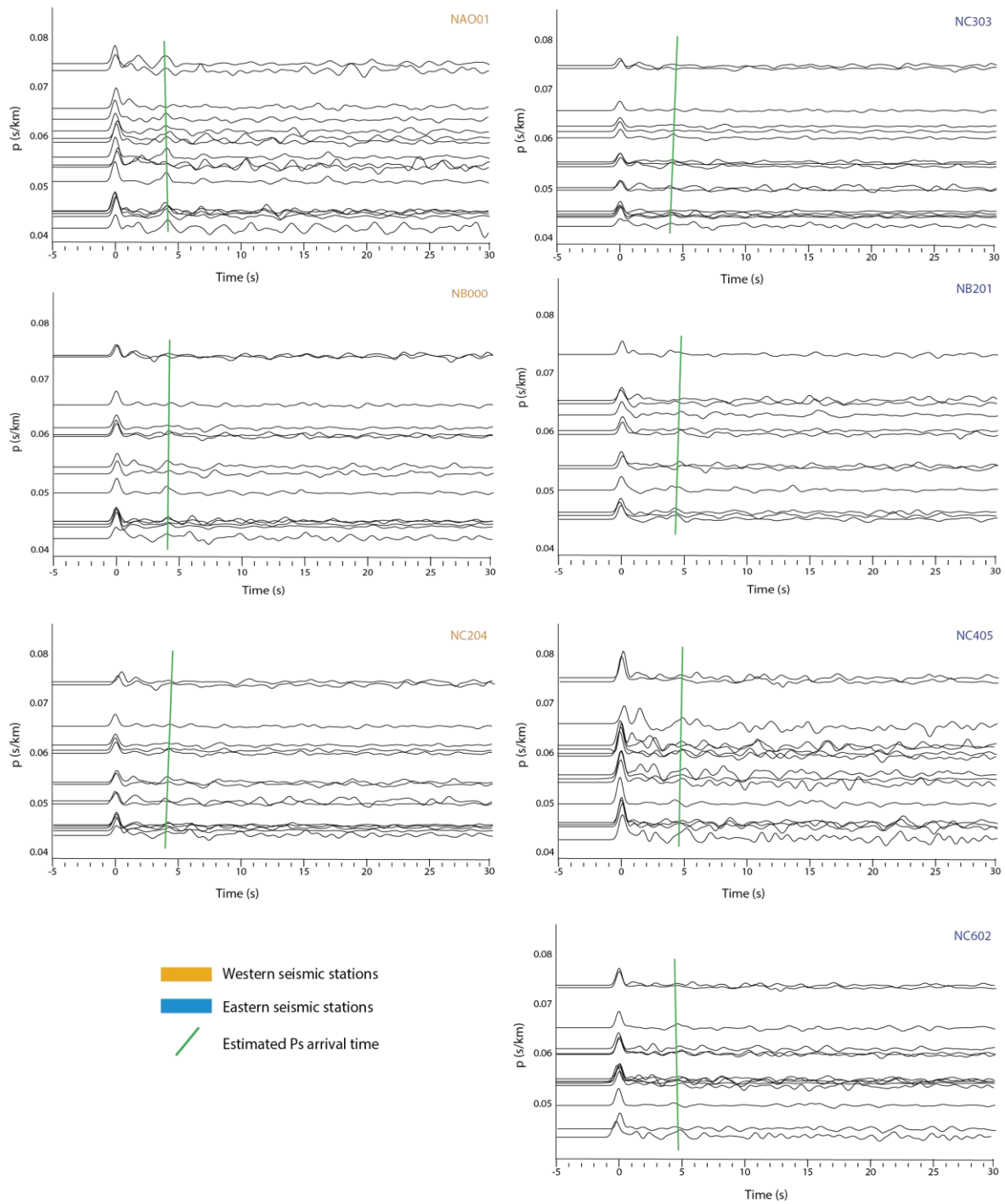
*Figure S1: Receiver functions travel time vs ray parameter **p** for all seismic stations. Individual receiver functions were obtained using an iterative time domain deconvolution (Ligorria & Ammon, 1995) and the ray parameter was calculated per each event using the UDTDD script available in the CPS package (Hermann, 2013). Green lines show tentative arrival times for Ps phase.*
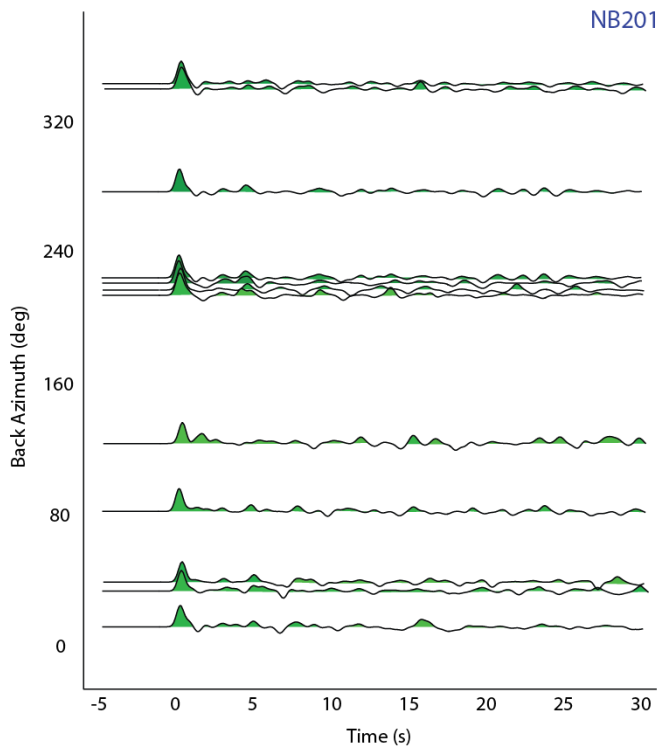
*Figure S2: Receiver functions travel time vs back azimuth for station NB201. Individual receiver functions were obtained using an iterative time domain deconvolution (Ligorria & Ammon, 1995) and the back azimuth was automatically calculated by SAC.*

The inversion process involves the calculation of several models which are inside a model space defined by the input parameters (see Table 2 in the main text). According this, credible ranges for the value of Vs versus depth are created. The maximum credible values are delimited by the 95% credible range, i.e 5% of the values are above this line. In the same way, the minimum credible values are restricted by the 5% credible range, which means that the 5% of the values are below this line. To illustrate this, the model space for the 5-layers model is presented (Figure S3).
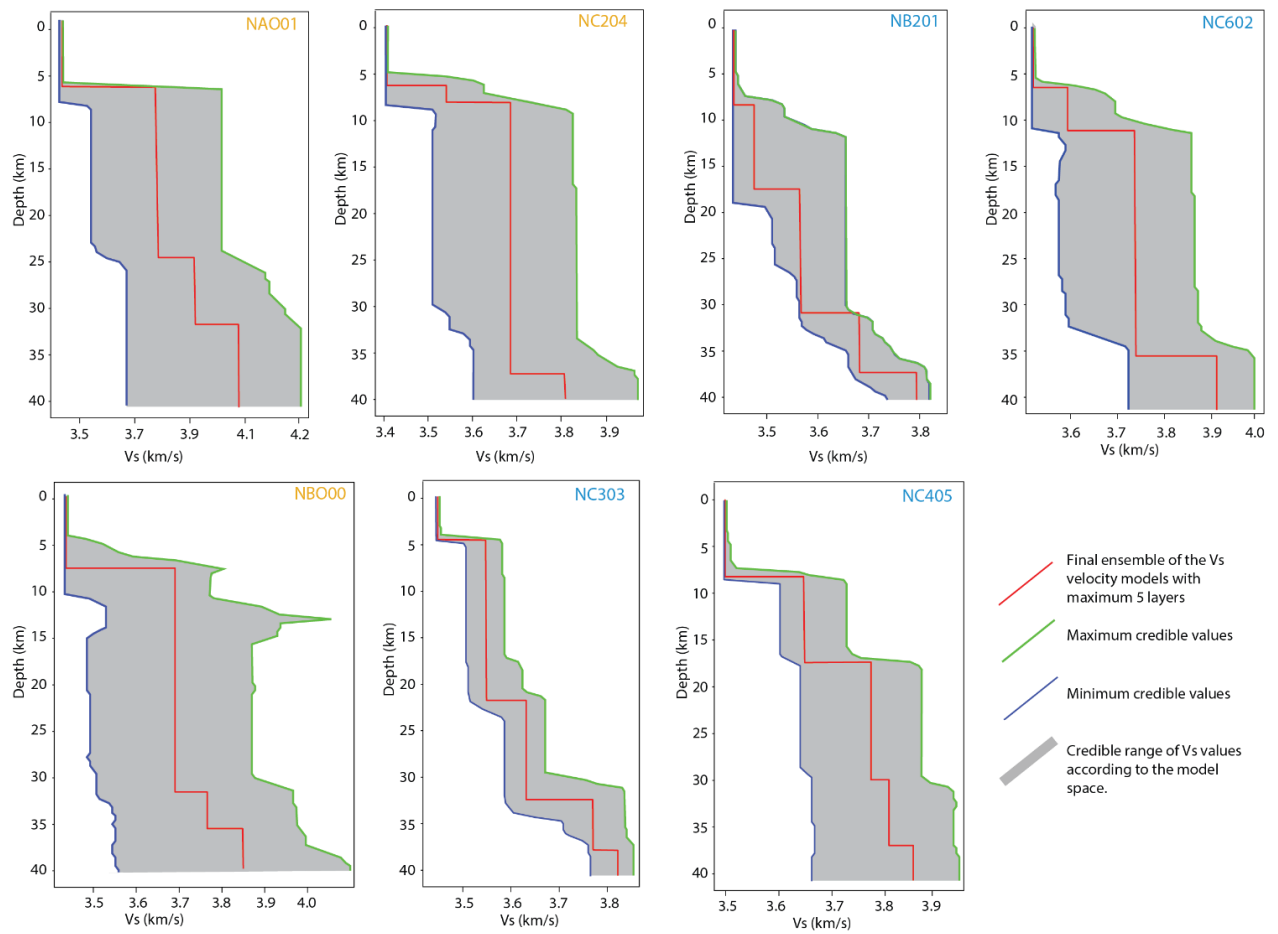


*Figure S3: 1D S-wave velocity models delimiting the model space for all seismic stations. The gray shaded area shows the entire sampled model space. The colored lines represent the minimum credible values, the ensemble solution and the maximum credible values in blue, red and green, respectively.*

GEOLOGICAL
SURVEY OF
NORWAY

· NGU ·